UNIVERSIDADE FEDERAL DE PERNAMBUCO
DEPARTAMENTO DE FÍSICA – CCEN
PROGRAMA DE PÓS-GRADUAÇÃO EM FÍSICA

DISSERTAÇÃO DE MESTRADO

NON-NEWTONIAN FLUIDS IN A HELE-SHAW CELL:
A PATTERN FORMATION STUDY

João Vitor Nogueira Fontana

Recife - PE, Brasil
Janeiro - 2014

UNIVERSIDADE FEDERAL DE PERNAMBUCO
DEPARTAMENTO DE FÍSICA – CCEN
PROGRAMA DE PÓS-GRADUAÇÃO EM FÍSICA

DISSERTAÇÃO DE MESTRADO

NON-NEWTONIAN FLUIDS IN A HELE-SHAW CELL: A PATTERN FORMATION STUDY

por

João Vitor Nogueira Fontana

Dissertação apresentada ao Programa de Pós-Graduação em Física do Departamento de Física da Universidade Federal de Pernambuco como parte dos requisitos para obtenção do título de Mestre em Física.

Banca Examinadora:
Prof. José Américo de Miranda Neto (Orientador, DF-UFPE)
Prof. Fernando Roberto de Luna Parisio Filho (DF-UFPE)
Prof. Fernando Jorge Sampaio Moraes (DF-UFPB)

Recife - PE, Brasil
Janeiro - 2014

Catalogação na fonte
Bibliotecário Jefferson Luiz Alves Nazareno, CRB 4-1758

Fontana, João Vitor Nogueira.
Non-newtonian fluids in a Hele-Shaw cell: a pattern formation study. / João Vitor Nogueira Fontana. – Recife: O Autor, 2014.
71 f.: fig., tab.

Orientador: José Américo Miranda Neto.
Dissertação (Mestrado) - Universidade Federal de Pernambuco. CCEN. Física , 2014.
Inclui referências e apêndice.

1. Dinâmica de fluídos. 2. Formação de padrões (ciências físicas). 3.Fluídos não-newtonianos. 4. Célula de Hele-Shaw. I.Miranda Neto, José Américo. (orientador). II. Título.

532.05 (22. ed.) FQ 2014-13

Universidade Federal de Pernambuco
Departamento de Física – CCEN
Programa de Pós-Graduação em Física
Cidade Universitária - 50670-901 Recife PE Brasil
Fone (++ 55 81) 2126-7640/2126-8449
http://www.ufpe.br/ppgfisica e-mail: posgrad@df.ufpe.br

Parecer da Banca Examinadora de Defesa de Dissertação de Mestrado

João Vitor Nogueira Fontana

NON-NEWTONIAN FLUIDS IN A HELE-SHAW CELL:
A PATTERN FORMATION STUDY

A Banca Examinadora composta pelos Professores José Américo de Miranda Neto (Presidente e Orientador), Fernando Roberto de Luna Parisio Filho, ambos do Departamento de Física da Universidade Federal de Pernambuco e Fernando Jorge Sampaio Moraes, do Departamento de Física da Universidade Federal da Paraíba, consideram o candidato:

(X) Aprovado ( ) Reprovado ( ) Em exigência

Secretaria do Programa de Pós-Graduação em Física do Departamento de Física do Centro de Ciências Exatas e da Natureza da Universidade Federal de Pernambuco, em trinta de janeiro de dois mil e catorze.

Prof. José Américo de Miranda Neto
Presidente e Orientador

Prof. Fernando Roberto de Luna Parisio Filho

Prof. Fernando Jorge Sampaio Moraes

I dedicate this work to my parents, who made me who I am.

Acknowledgements

Firstly I would like to thank my family for all the support it was given to me since I entered the undergraduate course until now. I also want to thank the person who influenced most deeply my manner to see science, my adviser and friend José Américo. I thank my friends Eduardo, Sérgio, Rebeca, Pablo, Victor, Chico and Luciano who discussed physics with me and made the perfect environment for my development in science. At last but not least, I thank my friends Manoel, Rodrigo, Nathalia and specially Malu for the pleasant moments I had with them during my entire academic life.

I don't want to evoke beliefs - I want to give suggestions and shake prejudices.

—SIGMUND FREUD (Gesammelte Schriften, Volume 7 - Page 250)

Resumo

A instabilidade de Saffman-Taylor se dá na interface entre dois fluidos viscosos no interior de uma célula de Hele-Shaw (CHS). A CHS é um aparato experimental que consiste em duas placas, usualmente planas e paralelas, separadas por uma distância muito pequena. Sabe-se que quando um fluido viscoso desloca outro mais viscoso, em uma CHS, a interface entre eles se torna instável e estruturas chamadas de "dedos viscosos" surgem. Em função da geometria da CHS e da força motriz do fluxo, tais dedos podem bifurcar, afinar, competir em tamanho e interferirem uns com os outros, formando as mais diversas estruturas morfológicas. Estudos com fluidos newtonianos em CHS vêm sendo feitos desde o final do século XIX. No entanto, apenas recentemente, a cerca de trinta anos, estudos com fluidos não newtonianos em CHS vêm sendo conduzidos, e em sua maioria estudos analíticos lineares ou não lineares puramente numéricos. Este trabalho tenta preencher essa lacuna com um estudo analítico não linear de fluidos não newtonianos em CHS. Estudamos a CHS de geometria radial com levantamento da placa superior e injeção como forças motrizes do fluxo. Nestes casos estudamos o fluido *yield stress*, um tipo especial de fluido não newtoniano que se comporta como um "semissólido". Estudamos também o fluido *power-law* que introduz, na viscosidade, uma dependência do fluxo. Em cada caso fomos capazes de estabelecer conexões entre as nossas previsões teóricas e os experimentos e simulações encontrados na literatura. Tais previsões são acerca da estabilidade e morfologia da interface como: bifurcação de dedos, a estrutura conhecida como *side branching* e a competição entre dedos.

Palavras-chave: Célula de Hele-Shaw, fluido não newtoniano, fluido *yield stress*, fluido *power-law*, competição de dedos viscosos, *side branching*.

Abstract

The Saffman-Taylor instability arises at the interface between two viscous fluids in a Hele-Shaw cell (HSC). A HSC is an experimental apparatus that consists of two plates, usually flat and parallel, separated by a very small distance. It's known that when a less viscous fluid displaces a more viscous one, in a HSC, the interface between them becomes unstable and the so called "viscous fingers" arise. Due to the geometry of the HSC and the driving force of the flux, such fingers can bifurcate, become narrow, compete in size and interfere with each other creating the most diverse morphological structures. Studies with Newtonian fluids in HSC have been made since the end of the XIX century. However, only recently, about thirty years ago, studies with non-Newtonian fluids in HSC have been conducted, mostly addressing linear analytical studies or nonlinear purely numerical ones. The work exposed in this dissertation intends to fill this gap with a nonlinear analytical study of non-Newtonian fluids in HSC. In this work we have studied the radial geometry HSC with the lifting of the upper plate and injection as the driving forces. In these cases we have studied the yield stress fluid, a special kind of non-Newtonian fluid that behaves as a "semi-solid". We have also studied the power-law fluid that introduces, in viscosity, a dependence on the flux. In each case we were capable of establish connections between our theoretical predictions and the experiments and simulations found in the literature. Such predictions are about the stability and morphology of the interface: finger bifurcation, the structure called side branching, and the competition between fingers.

Keywords: Hele-Shaw cell, non-Newtonian fluid, yield stress fluid, power-law fluid, viscous finger competition, side branching.

List of Figures

List of Tables

Contents

CHAPTER 1

Introduction

1.1 Pattern formation

We all observe the beautiful patterns present in nature: the colors in the wings of a butterfly, the stripes of a zebra, the shape of a snowflake or the shell of a snail [see Fig. 1.1]. It makes us wonder why and how they occur. The answer to these type of questions can be very complex and pass through many fields of science as mathematics [1], physics [2] and biology [3, 4].

Figure 1.1 Beautiful patterns found in nature. From left to right and top to bottom: butterfly, shell of snail, snowflake, zebra, coral, and fish.

One way to start answering questions about pattern shape and form is to try to understand the mechanisms behind their formation. Besides the aesthetic and academic interest, the understanding of pattern formation can be useful to industrial and technological applications [5].

Keeping all of that in mind, we try to gain some analytical insight on the mechanism of pattern formation. In this work, we are going to explore the formation of patterns at the interface

between fluids. Such interfacial patterns, as shown in Fig. 1.2, are the result of the development of hydrodynamic instabilities [2].

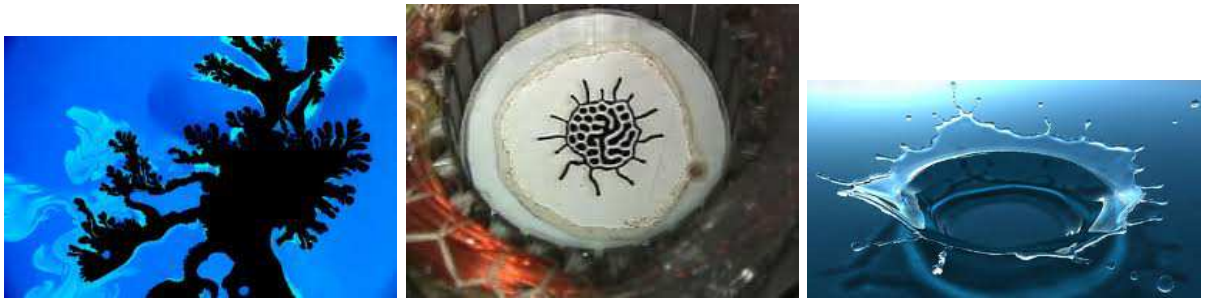

Figure 1.2 Interfacial fluid instabilities: Diffusion, magnetic fluid, water-air interface.

1.2 The classical Saffman-Taylor instability

To study hydrodynamic instabilities we are going to use the Hele-Shaw cell (HSC). In a HSC the fluids are confined in a quasi-two-dimensional geometry. The classical cell consists in two parallel plane plates separated by a very small distance, but there are many other HSC with curved and non-parallel plates. Such a cell was developed by Henry Selby Hele-Shaw. In 1885 Hele-Shaw was invited to organize the Department of Engineering at the University College Liverpool (founded in 1881), his second department, where he served as a Professor of Engineering until 1904 when he moved to South Africa. During this period Hele-Shaw carried out his seminal experiments at University College Liverpool, designing the cell that bears his name.

The particular hydrodynamic instability which we are interested in this work is the Saffman-Taylor instability: it arises at the interface separating two fluids in the confined geometry of a HSC. The Saffman-Taylor problem appeared in 1956 when Sir Geoffry Taylor and Philip G. Saffman used the HSC to model a problem in oil recovery industry. The physical mechanism used to extract oil from the oil well is to inject water in some point of the well and recover oil from another point. The well is a porous media and the equation describing flow in a porous media is, within some approximations, the same as the one that describes the flow in a HSC, the Darcy's law. In their work [2] Saffman and Taylor have shown that when a less viscous fluid displaces a more viscous one the interface separating them tends to destabilize and structures called "viscous fingers" start to grow [see Fig. 1.3]. This is similar to the oil recovery situation, where water (less viscous fluid) displaces oil (more viscous fluid) in a porous media and when the fingers start to grow, and a fraction of the oil remains in the well after the water reaches the extraction point.

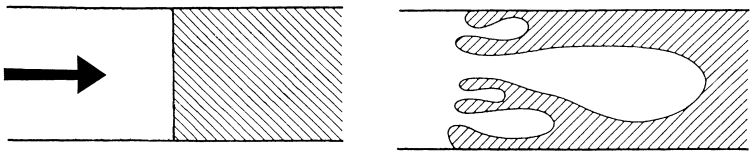

Figure 1.3 Development of a viscous finger. A less viscous fluid (in white) displaces the more viscous one (crosshatched).

1.3 Rheological behavior of fluids

The specific morphology of the patterns formed in a HSC depend on the nature of the fluids, on the geometry of the flow and on its driving force. Most of the existing studies on the viscous fingering instability refer to Newtonian fluids. In this case, the resulting interfacial shapes range from a single, smooth, steady-state finger in rectangular (or, channel) geometry [6–14], to multi-fingered structures in which repeated tip-splitting produces highly ramified patterns in the radial flow setup [15–26]. These pattern forming phenomena have been extensively studied during the last fifty years through analytical calculations, numerical simulations, and experiments.

Although not as numerous as in the Newtonian fluid case, other Hele-Shaw flow investigations have revealed that a distinct variety of patterns can be formed when one of the fluids is non-Newtonian [27]. While Newtonian fluids are characterized by a constant viscosity, non-Newtonian fluids display a multiplicity of hydrodynamic behaviors ranging from elasticity and plasticity to shear thinning and shear thickening, and in general have a shear-dependent viscosity.

Before we start to talk about rheology of fluids we have to define some important quantities such as viscosity, shear stress and rate of strain. The rate of strain is a quantity that measures how much the velocity changes along some direction and can be written as

$$e_{ij} = \frac{1}{2}\left[\frac{\partial u_i}{\partial x_j} + \frac{\partial u_j}{\partial x_i}\right], \tag{1.1}$$

with $\mathbf{u}$ being the velocity vector: $\mathbf{e} = [\boldsymbol{\nabla}\mathbf{u} + (\boldsymbol{\nabla}\mathbf{u})^T]/2$ is the rate-of-strain tensor, and T denotes matrix transposition. The shear stress tensor $\boldsymbol{\tau}$ is a quantity that contains all the information about shear stress in such a way that the shear stress on a surface defined by a normal vector $\boldsymbol{e}_i$ is given by

$$\boldsymbol{t}_i = \boldsymbol{e}_i \cdot \boldsymbol{\tau}. \tag{1.2}$$

For the Newtonian case the shear stress is proportional to the rate of strain and its constant of proportionality η is called viscosity.

We can classify fluids through their rheological behavior. Rheology is the study of the flow of matter, primarily in the liquid state, but also in solids under conditions in which they respond with plastic flow rather than deforming elastically in response to an applied force. It applies

to substances which have a complex microstructure, such as muds, sludges, suspensions, polymers and other glass formers (e.g., silicates), as well as many foods and additives, bodily fluids (e.g., blood) and other biological materials or other materials which belong to the class of soft matter. We classify the rheology of a material by relating the strain rate to the shear stress applied, as shown in Fig. 1.4.

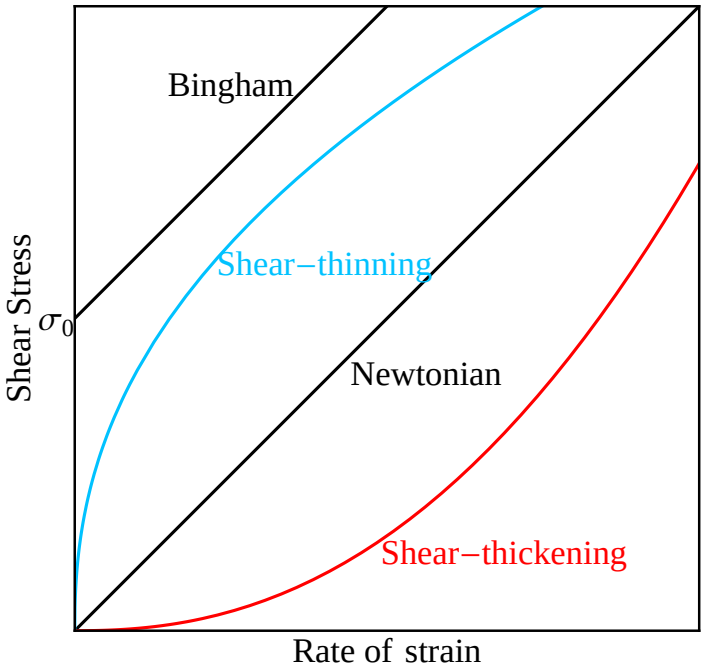

Figure 1.4 Flow curve for the Newtonian and non-Newtonian fluids discussed in this work: Newtonian, Bingham fluid, shear-thinning and shear-thickening.

The simplest rheological behavior is the linear one, where the the rate of strain grows linearly with the shear stress. The viscosity, derivative of the shear stress with respect to the rate of strain, in this case is constant. Since it was proposed by Newton, its name is Newtonian behavior. The Newtonian behavior explains, roughly, a great part of the fluids, but its general inaccuracy leads us to search for more complex behaviors, the so called non-Newtonian behaviors. We have, for example, the yield stress fluid that can be modelled by the Bingham plastic fluid model, that in contrast to Newtonian fluids can support shear stresses without flowing. As long as the stress remains below a certain critical value σ_0 they do not flow, but respond elastically to deformation and after that critical value it flows as a Newtonian fluid. So, such materials possess properties of both viscous fluids and elastic solids, behaving like a “semi-solid". Other simple forms of non-Newtonian behavior are the shear-thinning, where an increase in the shear stress causes a decreases in viscosity, and shear-thickening, where an increase in the shear stress causes an increases in viscosity. This dependence gives the flow curve a convex or concave profile. In this dissertation we are going to work with those three

non-Newtonian fluids in comparison to Newtonian fluids. In table 1.1 we can see examples of such fluids.

Rheology	**Example**
Newtonian (approximately)	Water, air, thin motor oil
Yield stress	Mud, toothpaste, slurry, mayonnaise
Shear-thinning	Lava, ketchup, blood, nail polish, whipped cream
Shear-thickening (less common)	Cornstarch + water (oobleck), soaked sand + water

Table 1.1 Examples of Newtonian and non-Newtonian fluids.

The rheological properties of non-Newtonian fluids exert a profound effect on the shape of the emerging interfacial patterns in Hele-Shaw flows. Rectangular and radial Hele-Shaw experiments involving non-Newtonian fluids like polymer solutions, liquid crystals, clays and foams unveiled pattern morphologies presenting snowflake-like shapes [28] and fracturelike structures [29, 30]. For shear-thinning fluids traditional finger tip-splitting events are inhibited, and the appearance of dendritic patterns with side branching is favored. Cracklike patterns presenting angular branches and sharp tips have also been found. One can see some of those patterns in Fig. 1.5. On the other hand, flow with shear-thickening fluids [31] displays patterns similar to those found in Newtonian fluids but with either narrowing or widening of the fingers, which can present asymmetric humps. This morphological diversity and rich dynamical behavior motivated a number of theoretical studies of the problem through linear and weakly nonlinear analyzes, and sophisticated numerical simulations [32–41].

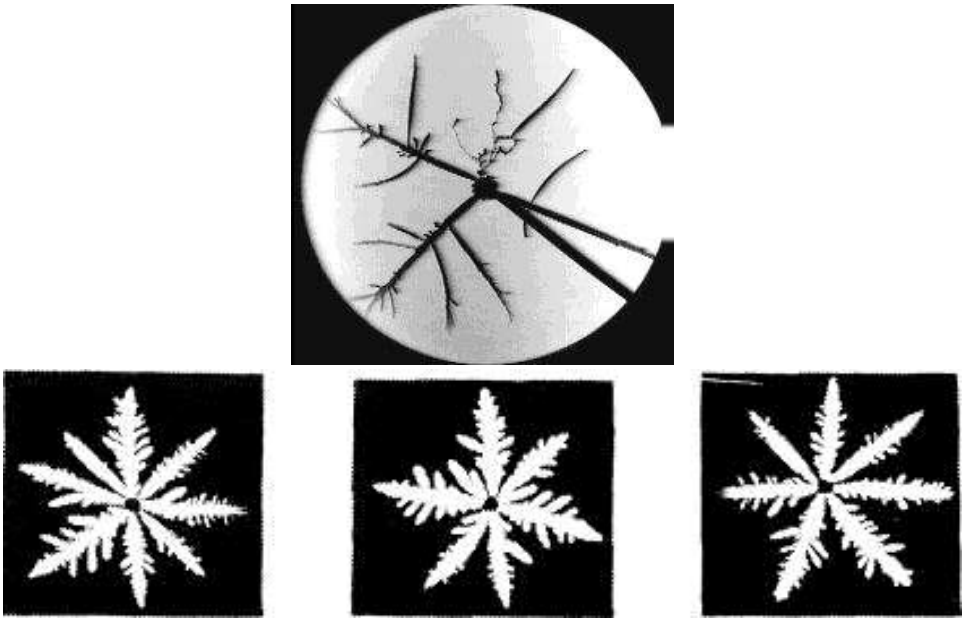

Figure 1.5 Typical morphological patterns in HSC with non-Newtonian fluids. Fracturelike pattern on the top, and side branching pattern on the bottom.

1.4 Yield stress fluids in a HSC

1.4.1 Injection-driven flow

Despite all the efforts and important results obtained by researchers on the development of viscous fingering in non-Newtonian Hele-Shaw flows, the pattern forming dynamics with yield stress fluids [42–44] has been relatively underlooked. On the theoretical side, a linear stability analysis of the Saffman-Taylor problem in rectangular and radial cells with yield stress fluids [45] has predicted that the instability can be drastically modified. On the experimental arena some interesting findings have been disclosed in channel geometry [46, 47]: depending on whether viscous effects or yield stresses dominates, fractal patterns, or ramified structures, where multiple fingers propagate in parallel, may arise.

In a more recent experimental work [48] fingering in a yield stress fluid in rectangular as well as in radial Hele-Shaw cells has been examined. As in Ref. [46,47] different regimes, leading to diverse pattern morphologies have been observed: at low velocities (where yield stress dominates) ramified structures arise; however, for higher velocities (viscous effects prevail), in addition to tip-splitting, interesting side branching instabilities become apparent. Although the behavior at the low velocity regime can be quantitatively explained from the linear stability results presented in Ref. [45], the nonlinear side branching and tip-splitting instabilities detected at higher velocities are not fully understood to date. So, a theoretical study addressing these suggestive pattern forming phenomena in yield stress fluids is still lacking. In this spirit, we will investigate such a problem in chapter 2.

1.4.2 Lifting-driven flow

An interesting variation of the traditional radial Saffman-Taylor problem [49] is the study of interfacial instabilities in HSC presenting variable gap-spacing [see Fig. 1.6]. The lifting Hele-Shaw problem occurs when the upper cell plate is lifted, while the lower plate remains at rest [50]. In this lifting flow configuration the inner fluid is viscous (e.g., oil), surrounded by an outer fluid of negligible viscosity (for instance, air). The lifting forces the fluid-fluid interface to move inwards. Consequently, the interface becomes unstable leading to the formation of a distinct class of fingering patterns [51–58].

In contrast to the injection-driven radial viscous flow situation where finger tip-splitting is the prevalent pattern forming mechanism [22, 25, 26, 49], a salient morphological aspect in lifting H-S flows is finger competition. Numerical simulations and experiments [50–56] reveal a strong competition (i.e. finger length variability) among the fingers of the invading less viscous fluid, which advance towards the center of the cell, as we can see in Fig. 1.7. It is also observed that the outermost limit of the interface ceases to shrink, indicating that the competition among the fingering structures of the more viscous fluid is considerably less intense.

The characteristic features of the finger competition dynamics described above are detected in laboratory and numerical experiments when the inner fluid is Newtonian [50–56]. It is true that depending on the nature of the viscous fluid used, different types of interfacial patterns arise [52, 57, 58]. Nevertheless, inspection of the experimental patterns obtained in

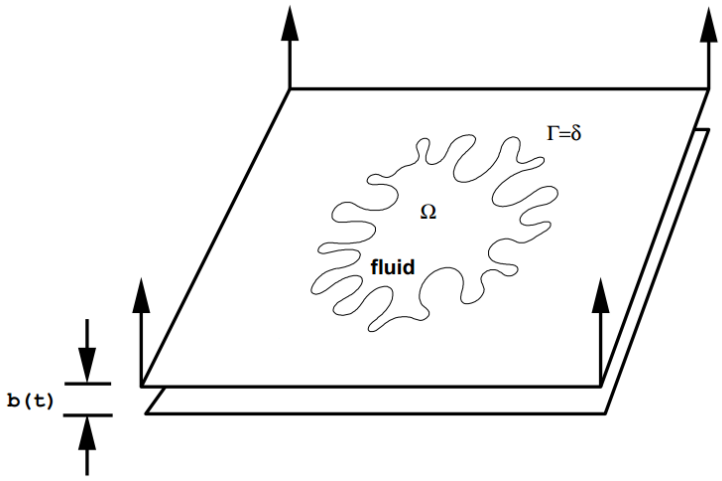

Figure 1.6 Schematic configuration of lifting-driven flow in a HSC, extracted from Ref. [50]. A blob of viscous fluid surrounded by air is invaded by fingers when the upper cell plate is lifted.

Ref. [52] seems to indicate that finger competition phenomena somewhat analogous to those found in Newtonian fluids, also occurs when the invaded fluid is non-Newtonian. Specifically, in Ref. [52] this happens when the stretched material is a yield stress fluid. Despite the existence of some theoretical works which analyze the development of finger competition in miscible [59] and immiscible [60] lifting HS flows with Newtonian fluids, a corresponding theoretical investigation focusing on the finger competition behavior in yield stress fluids has not been performed. We will investigate this aspect of the problem in chapter 3.

It has been recently shown [55] that in addition to the material parameters (viscosity, surface tension, etc.) of the fluids involved in lifting HS flows, a purely geometric factor plays an important role in determining pattern shape and evolution. Such a parameter is the aspect ratio, that expresses the ratio of the initially unperturbed, circular radius of the fluid-fluid interface to the initial HS plate spacing. Within this context, the aspect ratio measures the cell confinement. The experiments performed in [55] for Newtonian fluids demonstrated that the size and number of growing fingers are significantly sensitive to changes in the aspect ratio. Therefore, one facet of the lifting HS problem that deserves a closer investigation is the influence of the aspect ratio on the finger competition dynamics. This can be done by considering that the inner fluid is either Newtonian or yield stress. A comparative study of the finger competition responses of these fluids during the lifting process is also of interest, and will be investigated in chapter 3.

1.5 Controlling instabilities in power-law fluids in a HSC

Although the viscous fingering problem in Hele-Shaw cells has become one of the simplest yet most illuminating paradigms of interfacial pattern formation, depending on the situation the development of interfacial instabilities can be undesirable. One emblematic example in which the emergence of viscous fingering instability is clearly counterproductive is oil recovery [61].

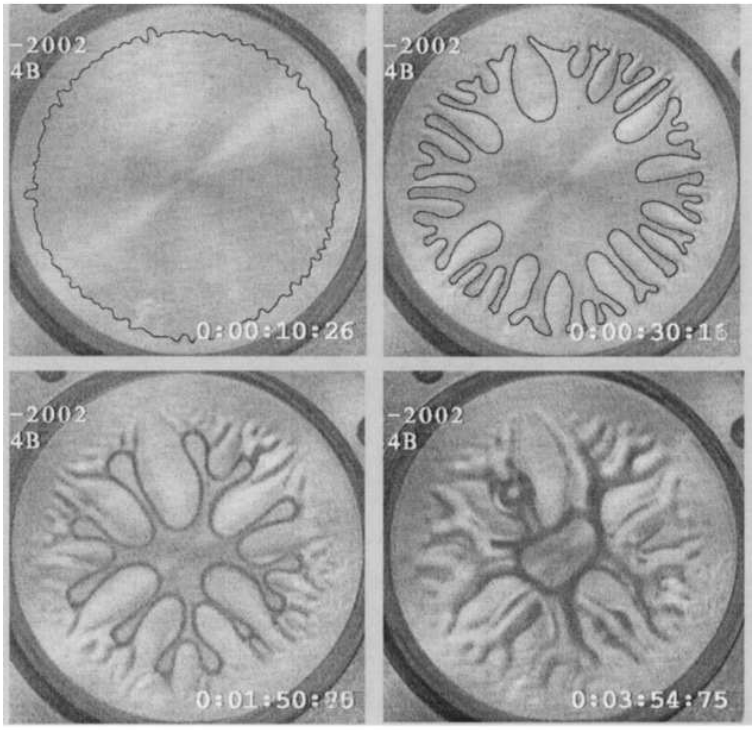

Figure 1.7 Experiment on lifting HSC, extracted from Ref. [52]. Time evolution of the fingers in the lifting-driven flow: we can see competition of the inward moving fingers, and at a later time the recircularization phenomena.

In this context, the viscous fingering instability is a major source of poor oil recovery, once rapidly evolving ramified fingers may reach the entrance of the well, and mainly water, and not oil is retrieved. It is also known that viscous fingering has a potentially harmful character in chromatographic separation [62, 63]. In addition, fingering instabilities are also unwanted in applications involving coatings [64, 65] and adhesives [53, 55]. So, processes aimed towards minimizing the fingering instabilities, or controlling the growth of viscous fingers are of technological and scientific importance.

A recent emerging research area concerns the buildup of controlling strategies to the viscous fingering instability problem. Due to its academic and practical relevance this particular topic has attracted the attention of engineers, physicists, and mathematicians [26, 66–77]. An interesting type of controlling scheme focuses on determining the number of fingers by properly adjusting the flow injection rate [26, 66–69]: instead of using the usual constant injection rate Q (area covered per unit time), which results in finger proliferation, these studies employ a time-dependent injection flux $Q(t) \sim t^{-1/3}$. As long as the injection rate presents this specific time dependence, the system evolves by keeping fixed the number of interfacial fingers [see Fig. 1.8]. It has been demonstrated that under such time-dependent flow rate the system always evolves into well behaved n-fold symmetric structures [26]. Even though this particular process was not able to eliminate the interfacial disturbances, it does offer a valid way to prescribe and control the morphology of the resulting patterns, avoiding the appearance of inconvenient

branched morphologies.

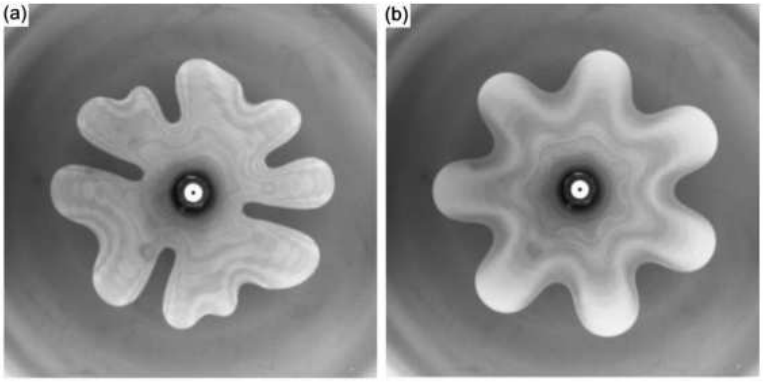

Figure 1.8 Patterns in a injection-driven HSC: (a) constant Q, (b) $Q(t) \sim t^{-1/3}$. We can clearly see the well-defined 7-fold symmetry in (b), where the finger branch is avoided. Figure extracted from Ref. [67].

An alternative line of research [70–77] seeks for mechanisms that are capable not only to restrain branched pattern formation, but that also inhibit the establishment of interfacial deformations. In this framework the main goal would be to obtain front propagation in the form of nearly stable, axisymmetric interfaces. This has been achieved by a couple of different procedures: first, by utilizing a two-stage piecewise constant injection process which applies a relatively low injection rate followed by a proper, stronger injection stage [70]. Another suppression method [72–74] employs a standard constant pumping rate Q, but substitutes the originally rigid Hele-Shaw upper plate with an elastic membrane. In this case, the onset of instability is deferred due to the membrane elastic distortions which reduce destabilizing pressure perturbations. Additional investigations [75–77] have shown that the introduction of a small gradient in the gap of the Hele-Shaw cell (tapered cell geometry), so that the rigid plates are not exactly parallel, can suppress the usual viscous fingering instability. In the limit of small taper angles, the dominantly stabilization mechanism is through variable transverse curvature (i.e. capillary effects).

Finally, it has been proposed that one could even optimally minimize the rising of any sort of interfacial disturbances via a variational method [71]. This variational scheme allows one to systematically search for the particular $Q(t)$ that leads to ideal minimization of the viscous fingering instability. It has been found that such an optimal injection rate varies linearly in time. The effectiveness of this particularly simple pattern formation controlling process has been substantiated by experiments and nonlinear numerical simulations in Ref. [71], as we can see in Fig. 1.9.

Interestingly, the studies mentioned above which tried to control the number of resulting interfacial fingers through a time-dependent injection rate [26,66–69], or that attempted to suppress or minimize the disturbances at the fluid-fluid interface [70–77] always consider the flow of *Newtonian* fluids. Therefore, a systematic theoretical investigation of similar controlling and minimizing protocols involving the displacement of non-Newtonian fluids still need to be addressed. This happens in spite of the fact that there is a considerable number of theoretical and experimental works that examine dynamics and pattern formation in Hele-Shaw cells in which

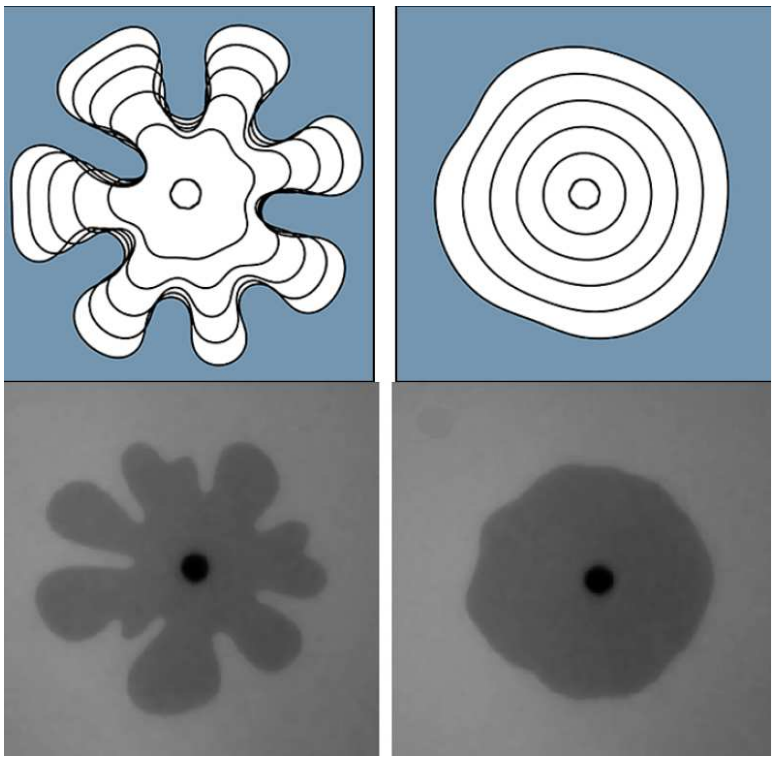

Figure 1.9 Figures extracted from Ref. [71]. Comparison of constant pumping rate (left panel) and their optimal pumping rate (right panel): simulations (top row) and experiments (bottom row). We can clearly see the efficiency of their controlling protocol.

the displaced fluid is non-Newtonian [28–41, 45–48, 78–82].

Considering the scientific and practical significance of non-Newtonian flows in Hele-Shaw geometry, in chapter 4 we examine the development of controlling and minimizing strategies in radial Hele-Shaw flows, now assuming that the displaced fluid is non-Newtonian. As in Ref. [41] we study a situation in which the dislocated fluid exhibits the simplest non-Newtonian rheology: a power-law viscosity. In this framing, we focus on understanding how the existing stabilization protocols for Newtonian fluids [26, 66–77] are modified by the fact that the displaced fluid can be either shear-thinning or shear-thickening.

Fortunately the work presented in the following three chapters has generated three publications in the periodic Physical Review E [78, 83, 84]. During this period, we have also another publication [85], not presented here, in the same periodic with the student Rodolfo Brandão.

CHAPTER 2

Injecting flow in a HSC with a yield stress fluid

2.1 Chapter outline

In this chapter we carry out the weakly nonlinear analysis of the problem in which a yield stress fluid flows, in a radial HSC, being pushed by an injected Newtonian fluid. We focus on the regime in which viscosity effects are prevalent over yield stress. By exploring the onset of nonlinear effects we try to gain analytical insight into the dynamic process of fingering formation. In particular, we seek to understand how mode-coupling dynamics leads to basic morphological features and behaviors observed experimentally in such non-Newtonian Hele-Shaw flows [48].

The rest of this chapter is organized as follows: Sec. 2.2 formulates the problem and derives a generalized Darcy-like law. In Sec. 2.3 we perform a Fourier decomposition of the interface shape, and from the alternative form of Darcy's law study the influence of weak yield stress effects on the development of interfacial patterns. Coupled, nonlinear, ordinary differential equations governing the time evolution of Fourier amplitudes are derived in detail. Section 2.4 discusses both linear and weakly nonlinear dynamics. It concentrates on the dawning of finger tip-splitting and side branching phenomena.

2.2 Problem formulation

In this chapter we are going to consider the displacement of a non-Newtonian yield stress fluid of viscosity η, surface tension γ and yield stress σ_0, by an injected Newtonian fluid of negligible viscosity in the confined geometry of a HSC. The schematic configuration of such physical system is depicted in Fig. 2.1. The surface tension between the fluids is denoted by γ. The Newtonian fluid is injected at a constant areal flow rate Q at the center of the cell, along the direction perpendicular to the plates (z-axis).

We focus on deriving the relevant hydrodynamic equation for a Hele-Shaw flow of a yield stress fluid. Our main goal is to obtain a Darcy's like law which relates the gap-averaged velocity with the pressure gradient and the yield stress, taking into account the coupling between them. We start by taking the Navier-Stokes equation for an incompressible viscous fluid [86]

$$\rho\left[\frac{\partial \mathbf{u}}{\partial t}+(\mathbf{u}\cdot\boldsymbol{\nabla})\mathbf{u}\right]=-\boldsymbol{\nabla}P-\boldsymbol{\nabla}\cdot\boldsymbol{\tau}, \tag{2.1}$$

where ρ is density, $\mathbf{u}$ denotes the three-dimensional velocity, P is the hydrodynamic pressure, and $\boldsymbol{\tau}$ represents the stress tensor that includes the yield stress [See Eq. (2.3)]. In the scope of

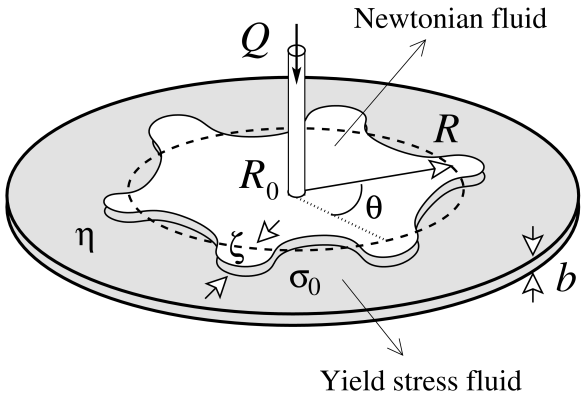

Figure 2.1 Schematic configuration of radial flow in a Hele-Shaw cell. The inner fluid is Newtonian and has negligible viscosity. The outer fluid is a yield stress fluid. The unperturbed fluid-fluid interface (dashed curve) is a circle of radius R. All physical parameters are defined in the text.

the lubrication approximation, where the distance between the plates b is much smaller than the unperturbed radius R of the fluid-fluid interface, the motion is a creeping flow. Therefore, we may neglect the inertial terms between square brackets in Eq. (2.1), as well as impose that the prevailing terms in $\boldsymbol{\nabla}\cdot\boldsymbol{\tau}$ are those with transversal derivatives. Within this framework, we also consider that pressure is constant along the transversal direction (z-axis). Thus, by integrating (2.1) we obtain

$$\tau_{iz} = \left|\frac{b}{2} - z\right| \nabla_i P, \tag{2.2}$$

where $i = r, \theta$ is the label that indicates polar radial or azimuthal components, with the origin placed at the center of the droplet. We have used the symmetry of the flow to state that the shear stress is zero at the mid-plane $z = b/2$ (since the plates are located at $z = 0$ and $z = b$). Furthermore, as a constitutive relation for yield stress fluids, we use the Bingham model [27]. It states that, for a given shear stress higher than the fluid yield stress magnitude σ_0, there is flow and the stress tensor is given by

$$\tau_{iz} = -\left[\eta\frac{\partial u_i}{\partial z} + \sigma_i\right]. \tag{2.3}$$

This situation corresponds to $|\boldsymbol{\tau}| > \sigma_0$, where $|\boldsymbol{\tau}| = \sqrt{\tau_{rz}^2 + \tau_{\theta z}^2}$. We point out that here we allow the yield stress to exhibit both r and θ polar components, in such a way that its response is opposite to the stress tension. This is precisely what will allow us to couple the yield stress to the velocity direction by the end of our derivation.

On the other hand, if $|\boldsymbol{\tau}| \leq \sigma_0$, the shear stress do not overcome the yield stress, thus there is no flow

$$\frac{\partial u_i}{\partial z} = 0, \tag{2.4}$$

meaning that $\sigma_i = -\tau_{iz}$.

We define the gap-averaged velocity as

$$\mathbf{v} = \frac{1}{b}\int_0^b \mathbf{u}\, dz, \tag{2.5}$$

Now we can use (2.1-2.5) to obtain a dimensionless modified Darcy's law for yield stress fluids

$$\mathbf{v} = -\boldsymbol{\nabla} P\left[1 - \frac{\delta}{|\boldsymbol{\nabla} P|} + \frac{4\,\delta^3}{27|\boldsymbol{\nabla} P|^3}\right]. \tag{2.6}$$

The dimensionless parameter

$$\delta = \frac{\pi\sigma_0 b R_f}{2\eta Q} \tag{2.7}$$

is a modified plasticity number, and quantifies the ratio between yield stress and viscous forces. For the remainder of this chapter, we take δ as positive (since Q > 0) and refer to it as the yield stress parameter. We point out that, in Eq. (2.6) lengths and velocities were rescaled by R_f and $Q/(2\pi R_f)$ respectively, where R_f is the radius of the unperturbed interface at $t = t_f$ [see Eq. (2.9)]. We refer the reader to Ref. [78] for more details on the derivation and validity of our modified Darcy's law model for yield stress fluids [Eq.(2.6)]. From this point on we use the dimensionless version of the equations. Our Eq. (2.6) is in agreement with the results of Ref. [87] which studied the simpler situation involving the purely radial flow of a perfectly circular droplet.

Since we are interested in examining the interface destabilization process, we consider the regime where viscous forces prevail over the yield stress and flow is facilitated, which corresponds to $\delta \ll 1$. Therefore, we may neglect the third order term in δ shown in Eq. (2.6). Moreover, since (2.6) states that velocity is parallel to the pressure gradient, we may rewrite it in a more convenient way as

$$\boldsymbol{\nabla} P = -\mathbf{v}\left[1 + \frac{\delta}{|\mathbf{v}|}\right]. \tag{2.8}$$

Equation (2.8) is an alternative form of Darcy's law ideally suited to describe the Hele-Shaw flow dynamics in the weak yield stress regime. The usual Newtonian Darcy's law is recovered when we set $\delta = 0$.

2.3 Mode-coupling equation

To perform the weakly nonlinear analysis of the system, we consider that the initial circular fluid-fluid interface is slightly perturbed [see Fig. 2.1], $\mathscr{R} = R(t) + \zeta(\theta,t)$ ($\zeta/R \ll 1$), where the time dependent unperturbed radius is given by

$$R(t) = \sqrt{R_0^2 + 2t}, \tag{2.9}$$

R_0 being the dimensionless unperturbed radius at $t = 0$. The interface perturbation is written in the form of a Fourier expansion

$$\zeta(\theta,t) = \sum_{n=-\infty}^{+\infty} \zeta_n(t)\exp(in\theta), \tag{2.10}$$

where $\zeta_n(t) = (1/2\pi)\int_0^{2\pi}\zeta(\theta,t)\exp(-in\theta)\,\mathrm{d}\theta$ denotes the complex Fourier mode amplitudes and n is an integer wave number. In our Fourier expansion (2.10) we include the $n=0$ mode to keep the area of the perturbed shape independent of the perturbation ζ. Mass conservation imposes that the zeroth mode is written in terms of the other modes as $\zeta_0 = -(1/2R)\sum_{n\neq 0}|\zeta_n(t)|^2$. We stress that our perturbation scheme keeps terms up to the second order in ζ and up to first order in δ.

The weakly nonlinear approach to radial, Newtonian Hele-Shaw flow developed in Ref. [25], related the fluid velocity to a *scalar* velocity potential $\mathbf{v} = -\boldsymbol{\nabla}\phi$, this replacement made possible by the irrotational nature of the flow for Newtonian fluids. For non-Newtonian yield stress fluids, in contrast, flows governed by the modified Darcy's law (2.8) exhibit vorticity. Hence, as in Ref. [39] we perform our calculations using a *vector* potential $\mathbf{v} = \boldsymbol{\nabla}\times\mathbf{A}$. The most general form of the vector potential can be written as

$$\mathbf{A} = \left[\theta + \sum_{m,n\neq 0} A_{mn}\left(\frac{R}{r}\right)^m \exp(in\theta)\right]\hat{\mathbf{z}}, \tag{2.11}$$

where A_{mn} are the Fourier coefficients of the velocity vector potential and $\hat{\mathbf{z}}$ is the outward unit-normal to the upper cell plate. The radial and polar components of the fluids velocities are

$$v_r = \frac{1}{r} + \sum_{m,n\neq 0} inA_{mn}\left(\frac{R^m}{r^{m+1}}\right)\exp(in\theta), \tag{2.12}$$

and

$$v_\theta = \sum_{m,n\neq 0} mA_{mn}\left(\frac{R^m}{r^{m+1}}\right)\exp(in\theta). \tag{2.13}$$

We exploit the fact that $\boldsymbol{\nabla}P$ must be curl free, $\boldsymbol{\nabla}\times\boldsymbol{\nabla}P = 0$. It simplifies the general form of the vector potential expansion given in Eq. (2.11). It also reveals that, without loss of generality, one can rewrite the vector potential as

$$\mathbf{A} \;=\; \left\{\theta + \sum_{n\neq 0} A_n\left(\frac{R}{r}\right)^{|n|}\exp(in\theta) \;+\; \delta\left[\sum_{n\neq 0} B_n\left(\frac{R}{r}\right)^{|n|} r\exp(in\theta)\right]\right\}\hat{\mathbf{z}}, \tag{2.14}$$

replacing the array of coefficients A_{mn} with the simpler set of A_n and B_n. Observe that the vector potential (2.14) is simply a superposition of a purely Newtonian term ($\propto \delta^0$, coefficients A_n) and a non-Newtonian contribution ($\propto \delta^1$, coefficients B_n)

$$\mathbf{A} = \mathbf{A}_N + \mathbf{A}_{NN}. \tag{2.15}$$

The flow described by $\mathbf{A}_N$ is irrotational, while $\mathbf{A}_{NN}$ has a curl.

Similarly, we express the pressure of the outer fluid as a sum of Newtonian and non-Newtonian pressures, and propose a general form for their Fourier expansion

$$P = P_N + P_{NN}, \tag{2.16}$$

where

$$P_N = -\log\left(\frac{r}{R}\right) + \sum_{n\neq 0} p_n \left(\frac{R}{r}\right)^{|n|} \exp(in\theta), \tag{2.17}$$

and

$$P_{NN} = \delta\left[-r + \sum_{n\neq 0} q_n \left(\frac{R}{r}\right)^{|n|} r\exp(in\theta)\right]. \tag{2.18}$$

The gradient of the complex pressure field (2.16) must satisfy the non-Newtonian Darcy's law given by Eq. (2.8). By inspecting the r and θ components of (2.8), and by examining the Newtonian and non-Newtonian components of it, we can express the Fourier coefficients of P_N, P_{NN} and $\mathbf{A}_{NN}$ in terms of the Fourier coefficients of $\mathbf{A}_N$,

$$p_n = i\mathrm{sgn}(n)\,(A_n)\,, \tag{2.19}$$

$$q_n = iA_n\mathrm{sgn}(n)\beta(n) + \sum_{m\neq 0, m\neq n} mA_m\,(n-m)A_{n-m}\,k\,(n,m)\,, \tag{2.20}$$

$$B_n = A_n\alpha(n) + \sum_{m\neq 0, m\neq n} m\,(iA_m)\,(n-m)A_{n-m}\,h\,(n,m)\,, \tag{2.21}$$

where in order to keep the results in a compact form, we introduced the coefficients

$$\alpha\,(n) = \frac{|n|\,(|n|-1)}{(2|n|-1)}, \tag{2.22}$$

$$\beta\,(n) = \frac{n^2}{(2|n|-1)}, \tag{2.23}$$

$$h(n,m) = \frac{1}{2|n|-1}\left[(1-|n-m|)\mathrm{sgn}(m) - 2(n-m) + \frac{n}{2}(1-\mathrm{sgn}[m(n-m)])\right], \tag{2.24}$$

and

$$k(n,m) = \frac{1}{n}\left[\mathrm{sgn}(m) - (|n|-1)h(n,m)\right]. \tag{2.25}$$

Note that $\mathrm{sgn}(n) = 1$ if $n > 0$ and $\mathrm{sgn}(n) = -1$ if $n < 0$.

Using Eqs. (2.19)-(2.21), which are consistent with the Darcy's law (2.8), we can relate the full expression of the velocity and pressure, up to first order in δ, with the coefficient A_n. Now we seek to express A_n in terms of the perturbation amplitudes.

To fulfill this goal, we consider the generalized pressure jump condition at the interface, that can be written as [49]

$$P|_{\mathscr{R}} = -\Gamma\,\kappa_{\|}|_{\mathscr{R}}, \tag{2.26}$$

and the kinematic boundary condition [22, 49]

$$\frac{\partial \mathscr{R}}{\partial t} = \left[\frac{1}{r}\frac{\partial \mathscr{R}}{\partial \theta}(-v_\theta) + v_r\right]_{|_{\mathscr{R}}}, \tag{2.27}$$

which states that the normal components of each fluid's velocity at the interface equals the velocity of the interface itself.

In (2.26)

$$\Gamma = \frac{b^2\pi\gamma}{6\eta R_f Q} \tag{2.28}$$

is a surface tension parameter, and $\kappa_{\|}$ is the curvature in the direction parallel to the plates.

By expanding Eqs. (2.26) and (2.27) up to the first order in ζ and $\dot{\zeta}$ and first order in δ we find the coefficient of the vector potential corresponding to the n-th evolution mode, $A_n^{(1)}$,

$$iA_n^{(1)}(t) = \left[\frac{R}{n}\dot{\zeta}_n + \frac{1}{nR}\zeta_n\right][1 - \delta R\alpha(n)], \tag{2.29}$$

where the overdot denotes total time derivative.

Now we can use Eqs. (2.26) and (2.29) to calculate, up to the second order in ζ and $\dot{\zeta}$ and first order in δ, the vector potential corresponding to the n-th evolution mode, $A_n^{(2)}$,

$$\begin{aligned} iA_n^{(2)}(t) &= \frac{1}{R}\sum_{m\neq n,0}\left[\frac{1}{2|n|R}\right. \\ &+ \frac{\Gamma}{|n|R^2}\left(2m^2 + \frac{m(n-m)}{2} - 1\right) \\ &+ \left.\delta u(n,m)\right]\zeta_m\zeta_{n-m} \\ &+ \sum_{m\neq n,0}\left[\frac{1}{n} + \delta R v(n,m)\right]\dot{\zeta}_m\zeta_{n-m} \\ &+ \delta R^3\sum_{m\neq n,0}\frac{k(n,m)}{|n|}\,\dot{\zeta}_m\dot{\zeta}_{n-m} \\ &+ \delta R\sum_{m\neq n,0}\frac{k(n,m)}{|n|}\,\zeta_m\dot{\zeta}_{n-m}, \end{aligned} \tag{2.30}$$

where the coefficients

$$u(n,m) = \frac{1}{|n|}\left\{k(n,m) + \left(1 - \frac{1}{|m|}\right)\beta(m) - \alpha(m) - \beta(n)\left[\frac{1}{2} + \frac{\Gamma}{R}\left(2m^2 + \frac{m(n-m)}{2} - 1\right)\right]\right\}, \tag{2.31}$$

$$v(n,m) = \frac{1}{|n|}\left[k(n,m)-\beta(n)+\left(1-\frac{1}{|m|}\right)\beta(m)-\alpha(m)\right]. \tag{2.32}$$

Finally, by using Eqs. (2.27), (2.29) and (2.30) one can find the equation of motion for the perturbation amplitudes ζ_n. We present the evolution of the perturbation amplitudes in terms of δ, ζ and $\dot{\zeta}$

$$\dot{\zeta}_n = \dot{\zeta}_n^{(1)} + \dot{\zeta}_n^{(2)}, \tag{2.33}$$

where

$$\dot{\zeta}_n^{(1)} = \lambda(n)\,\zeta_n, \tag{2.34}$$

$$\lambda(n) = \frac{1}{R^2}(|n|-1) - \frac{\Gamma}{R^3}|n|\left(n^2-1\right) + \delta\frac{|n|}{2|n|-1}\left[\frac{|n|-1}{R}+\frac{\Gamma}{R^2}|n|(n^2-1)\right] \tag{2.35}$$

is the linear growth rate, and

$$\begin{aligned}
\dot{\zeta}_n^{(2)} &= \sum_{m\neq n,0}\left[F_N(n,m)+\delta\, F_{NN}(n,m)\right]\,\zeta_m\zeta_{n-m} \\
&+ \sum_{m\neq n,0}\left[G_N(n,m)+\delta\, G_{NN}(n,m)\right]\,\dot{\zeta}_m\zeta_{n-m} \\
&+ \delta\sum_{m\neq n,0} H_{NN}(n,m)\,\zeta_m\dot{\zeta}_{n-m} \\
&+ \delta\sum_{m\neq n,0} J_{NN}(n,m)\,\dot{\zeta}_m\dot{\zeta}_{n-m}.
\end{aligned} \tag{2.36}$$

In Eq. (2.36) the coefficients $F_N, F_{NN}, G_N, G_{NN}, H_{NN}$, and J_{NN} represent the second order Newtonian (N) and non-Newtonian (NN) terms. These second order coefficients present special reflection symmetries $\mathscr{C}(n,-m) = \mathscr{C}(-n,m)$, and $\mathscr{C}(-n,-m) = \mathscr{C}(n,m)$, where $\mathscr{C} = F_N, F_{NN}, G_N, G_{NN}, H_{NN}$, and J_{NN}, as the reader can see in Eqs. (2.37)-(2.42). Such symmetries facilitate the analysis performed in subsection (2.4.2).

$$F_N(n,m) = \frac{|n|}{R^3}\left[\frac{1}{2}-\mathrm{sgn}(nm)-\frac{\Gamma}{R}\left(1-\frac{nm}{2}-\frac{3m^2}{2}\right)\right], \tag{2.37}$$

$$\begin{aligned} F_{NN}(n,m) &= \frac{1}{R^2}\Bigg\{ \left(2-\frac{n}{m}\right)\alpha(m) \\ &+ |n|\left[\frac{1}{2}-\frac{\Gamma}{R}\left(1-\frac{nm}{2}-\frac{3m^2}{2}\right)\right][\alpha(n)-\beta(n)] \\ &+ |n|\left[\left(1-\frac{1}{|m|}\right)\beta(m)-\alpha(m)\right]+f(n,m)\Bigg\}, \end{aligned} \tag{2.38}$$

$$G_N(n,m) = \frac{|n|}{R}\left[1-\mathrm{sgn}(nm)-\frac{1}{|n|}\right], \tag{2.39}$$

$$\begin{aligned} G_{NN}(n,m) &= \left(2-\frac{n}{m}\right)\alpha(m) \\ &+ |n|\left[\alpha(n)-\beta(n)+\left(1-\frac{1}{|m|}\right)\beta(m)-\alpha(m)\right] \\ &+ f(n,m), \end{aligned} \tag{2.40}$$

$$H_{NN}(n,m) = f(n,m), \tag{2.41}$$

$$J_{NN}(n,m) = R^2\, f(n,m), \tag{2.42}$$

$$f(n,m) = nh(n,m)+|n|k(n,m). \tag{2.43}$$

Equation (2.33) is the mode-coupling equation of the Saffman-Taylor problem with yield stress fluids in radial geometry. It gives us the time evolution of the perturbation amplitudes ζ_n, accurate to second order, in the weak yield stress limit. Notice that Eq. (2.33) is conveniently written in terms of two dimensionless parameters: δ [Eq. (2.7)] and Γ [Eq. (2.28)]. The generalized Darcy law (2.8) and the equation of motion (2.33) constitute central results of this chapter.

2.4 Discussion

We proceed by using our mode-coupling approach to investigate the interface evolution at first and second order in ζ. To simplify our discussion it is convenient to rewrite the net perturbation (2.10) in terms of cosine and sine modes

$$\zeta(\theta,t) = \zeta_0 + \sum_{n=1}^{\infty}\left[a_n(t)\cos(n\theta)+b_n(t)\sin(n\theta)\right], \tag{2.44}$$

where $a_n = \zeta_n + \zeta_{-n}$ and $b_n = i(\zeta_n - \zeta_{-n})$ are real-valued. Without loss of generality, for the remainder of this chapter, we choose the phase of the fundamental mode so that $a_n > 0$ and $b_n = 0$. Henceforth, we study the development of interfacial instabilities, and examine how the yield stress parameter δ and the effective surface tension Γ affect pattern morphology. It should be noted that the theoretical results presented in the following sections utilize dimensionless quantities which are extracted from the realistic physical parameters used in the experiments of Refs. [22–24] and [47, 48].

2.4.1 First order: Linear analysis

Before analyzing the weakly nonlinear regime, and try to understand how nonlinearity affects the morphology of the emerging patterns, we briefly discuss some useful information which can be extracted from the linear growth rate (2.35). The wave number of maximum growth [obtained by setting $d\lambda(n)/dn = 0$] for a Newtonian fluid ($\delta = 0$) can be easily calculated from Eq. (2.35), yielding

$$n_{max}^N = \sqrt{\frac{1}{3}\left(1 + \frac{R}{\Gamma}\right)}. \tag{2.45}$$

From Eq. (2.35), one can obtain an explicit solution for the wave number n_{max} with maximal growth rate for a yield stress fluid ($\delta \neq 0$). Although this expression is rather complex, in the limit $\Gamma \ll 1$ it simplifies to (see Appendix A)

$$n_{max} \approx n_{max}^N \left(1 + \frac{\delta R}{4}\right). \tag{2.46}$$

It is worth noting that a similar kind of approximation has been performed in Ref. [40], leading to their Eq. (62). We stress that this limit (very small Γ) is consistent with experimental data of Refs. [22–24] and [47, 48] which imply in Γ of the order of 10^{-3}. We have also verified that the critical wave number [obtained by setting $\lambda(n) = 0$], that is the maximum wave number for which the growth rate is still positive, is shifted towards higher wave numbers as the yield stress parameter δ is increased. These findings indicates that yield stress effects tend to destabilize the interface in the weak yield stress regime.

Further insight on the linear behavior can be obtained from Fig. 2.2 which plots $\lambda(n)$ as a function of mode number n for three different values of the yield stress parameter δ (0, 0.075, and 0.15), and $\Gamma = 4.45 \times 10^{-3}$. By examining Fig. 2.2, we notice that by increasing δ one observes an increased growth rate of the fastest growing mode n_{max}, so that it is shifted towards larger wave number values. Since n_{max} is related to the typical number of fingers formed at the onset of the instability, this means that higher δ would induce the formation of patterns tending to present an increased number of fingered structures. It is also clear that the action of yield stress widens the band of unstable modes. These linear stability results indicate that interfacial instabilities involving multi-fingered structures presenting finger tip-splitting and side branching would be plausible candidates to arise due to the action of yield stress effects.

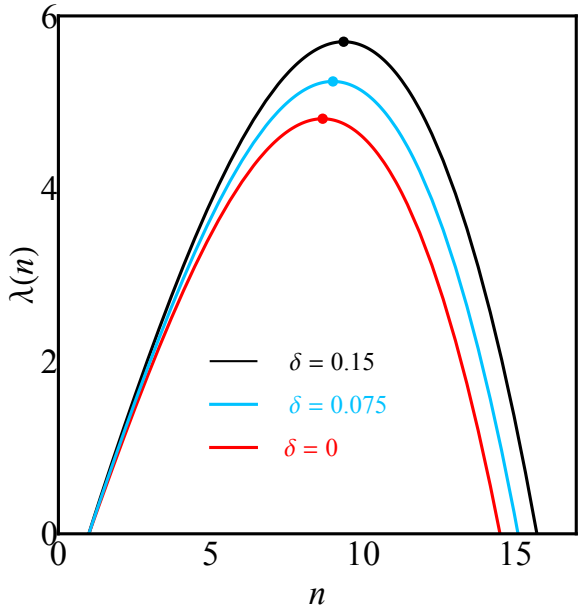

Figure 2.2 Linear growth rate $\lambda(n)$ as a function of mode n, for three values of δ, surface tension parameter $\Gamma = 4.45 \times 10^{-3}$, and $t = t_f = 0.495$. To better guide the eye the maxima of the curves are explicitly indicated by small dots.

2.4.2 Second order: Weakly nonlinear analysis

Now the mode-coupling equation (2.33) is utilized in its entirety to study the onset of pattern formation through the coupling of a small number of modes. Specifically, we will be interested in examining the action of the yield stress parameter δ on the mechanisms of finger tip-splitting and side branching. Such morphological structures were described in experimental works [46–48].

2.4.2.1 Tip-splitting mechanism

Within the scope of our mode-coupling theory, finger tip-splitting and finger tip-narrowing are related to the influence of a fundamental mode n on the growth of its harmonic $2n$ [25, 39]. For consistent second order expressions, we replace the time derivative terms $\dot{a}_n$ and $\dot{b}_n$ by $\lambda(n)\, a_n$ and $\lambda(n)\, b_n$, respectively. Under these circumstances the equation of motion for the cosine mode $2n$ is

$$\dot{a}_{2n} = \lambda(2n)\, a_{2n} + \frac{1}{2}\, T(2n,n)\, a_n^2, \tag{2.47}$$

where the tip-splitting function is given by

$$\begin{aligned} T(n,m) &= F_N(n,m) + \lambda(m)\, G_N(n,m) + \delta\, [F_{NN}(n,m) \\ &+ \lambda(m)\, G_{NN}(n,m) + \lambda(n-m)\, H_{NN}(n,m) \\ &+ \lambda(m)\, \lambda(n-m)\, J_{NN}(n,m)]. \end{aligned} \tag{2.48}$$

Equation (2.47) shows that the presence of the fundamental mode n forces growth of the harmonic mode $2n$. The function $T(2n,n)$ acts like a driving force and its sign dictates if finger tip-splitting is favored or not by the dynamics. If $T(2n,n) < 0$, a_{2n} is driven negative, precisely the sign that leads to finger tip-widening and finger tip-splitting. If $T(2n,n) > 0$ growth of $a_{2n} > 0$ would be favored, leading to outwards-pointing finger tip-narrowing.

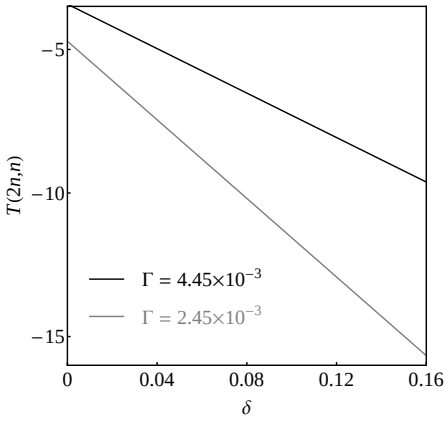

Figure 2.3 Tip-splitting function $T(2n,n)$ plotted against the yield stress parameter δ, for two values of the surface tension parameter Γ: 4.45×10^{-3}, and 2.45×10^{-3}. Here $t = t_f = 0.495$. Note that the qualitative behavior of $T(2n,n)$ is basically the same for the two values of Γ. As expected, for a given δ, smaller Γ leads to enhanced tendency towards finger tip-widening and splitting.

Figure 2.3 plots the behavior of $T(2n,n)$ as a function of δ, for two different values of the surface tension parameter Γ. To simplify our analysis we consider the onset of growth of mode $2n$ [using the condition $\lambda(2n) = 0$] in the Newtonian limit $\delta = 0$, where we know $T(2n,n)$ is negative [25]. By inspecting Fig. 2.3 we see that, regardless of the value of Γ, $T(2n,n)$ becomes more negative as δ increases, driving a_{2n} negative [see Eq.(2.47)]. Considering the presence of only modes n and $2n$ this indicates an enhanced tendency of the fingers to get wider, and possibly split. These second order results are consistent with the first order predictions described in section 2.4.1, which associated larger δ with finger proliferation.

It is important to notice that, although Fig. 2.3 indicates an increasing tendency to observe tip-splitting for larger values of δ and lower values of Γ, this is not sufficient to guarantee that finger tip-splitting will be the dominant morphological feature. It is necessary to analyze the interplay between the tip-splitting and other relevant nonlinear phenomena such as side branching in order to determine the ultimate shape of the evolving pattern. In the following section we investigate the role of the side branching mechanism in our system, and analyze which effect prevails for each set of dimensionless parameters.

2.4.2.2 Side branching mechanism

Another relevant non-Newtonian effect that can be studied at second order refers to the side branching phenomenon [39]. In the realm of a mode-coupling theory, side branching requires the presence of mode $3n$. If the harmonic mode amplitude a_{3n} is positive and sufficiently large, it can produce interfacial lobes branching out sidewards which we interpret as side branching.

As commented at the introduction of this work, an experimental study of radial Hele-Shaw flow with yield stress fluids (in the regime where viscous effects are prevalent over yield stress), detected the development of patterns exhibiting occasional tip-splitting and dominant side branching [48]. Taking these experimental facts into consideration we analyze the interplay of three modes: n, $2n$, and $3n$. More precisely, we examine the influence of the fundamental mode n, and its harmonic $2n$, on the growth of mode $3n$. The equation of motion for the cosine $3n$ mode is

$$\dot{a}_{3n} = \lambda(3n)\, a_{3n} + \frac{1}{2}\, S(3n)\, a_n a_{2n}, \tag{2.49}$$

where the side branching function $S(3n) = [T(3n,n) + T(3n,2n)]$ can be easily obtained from Eq. (2.48). By analyzing Eq. (2.49) we observe that mode $3n$ can be spontaneously generated due to the driving term proportional to $a_n a_{2n}$, such that it enters through the dynamics even when it is missing from the initial conditions. The existence and phase of mode $3n$ depends on the interplay of the modes n and $2n$. Side branching would be favored if $a_{3n} > 0$.

To study the growth of mode $3n$, in Fig. 2.4 we plot the function $S(3n)$ as the yield stress parameter is varied. Here, we consider the onset of growth of mode $3n$ [i.e. obeying the condition $\lambda(3n) = 0$] in the Newtonian limit $\delta = 0$. From Fig. 2.4 one can verify that $S(3n)$ is indeed negative for all values of δ. As shown in section 2.4.2.1, starting with a fundamental mode a_n, the harmonic mode a_{2n} is driven negative. Hence the product $S(3n)a_n a_{2n}$ in Eq. (2.49) is positive, driving $a_{3n} > 0$, exactly the sign that favors side branching. Of course, whether side branching actually occurs depends on the magnitude of a_{3n}.

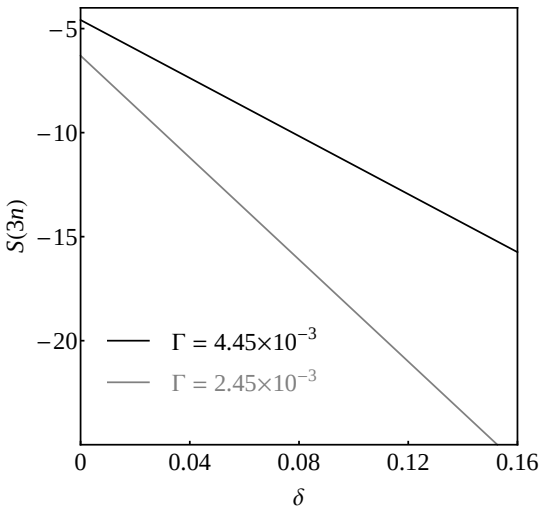

Figure 2.4 Behavior of the side branching function $S(3n)$ as the yield stress parameter δ is increased, for two values of the surface tension parameter Γ: 4.45×10^{-3}, and 2.45×10^{-3}. Here $t = t_f = 0.495$.

It is worth pointing out that there exists a subtle interconnection between modes $3n$ and $2n$, described by the evolution equation (2.49), and a similar expression for the growth of mode $2n$,

$$\dot{a}_{2n} = \lambda(2n)\, a_{2n} + \frac{1}{2}\, [T(2n,n)\, a_n^2 + S_{2n}\, a_n a_{3n}], \tag{2.50}$$

where $S_{2n} = [T(2n,-n) + T(2n,3n)]$ is positive, but decreases in magnitude as δ is increased. Hence, when $\delta = 0$ side branching via a positive a_{3n} will tend to drive a_{2n} less negative, diminishing the intensity of tip splitting but also, as a by-product, reducing a the growth rate of a_{3n} itself. Fortunately, these effects become less important when $\delta > 0$, so that side branching could still be detected by properly tuning δ and Γ.

The role of the yield stress parameter in determining the side branching behavior is illustrated in Fig. 2.5 which depicts the time evolution of the interface, plotted at equal time intervals, considering the interaction of three representative cosine modes: a fundamental $n = 4$ and its harmonics $2n = 8$, and $3n = 12$. The final time is $t = 0.495$, $R_0 = 0.1$, and $\Gamma = 4.45 \times 10^{-3}$. The initial amplitudes at $t = 0$ are $a_n = R_0/(32.5)$, $a_{2n} = 0$, and $a_{3n} = 0$, so that modes $2n$ and $3n$ are both initially absent.

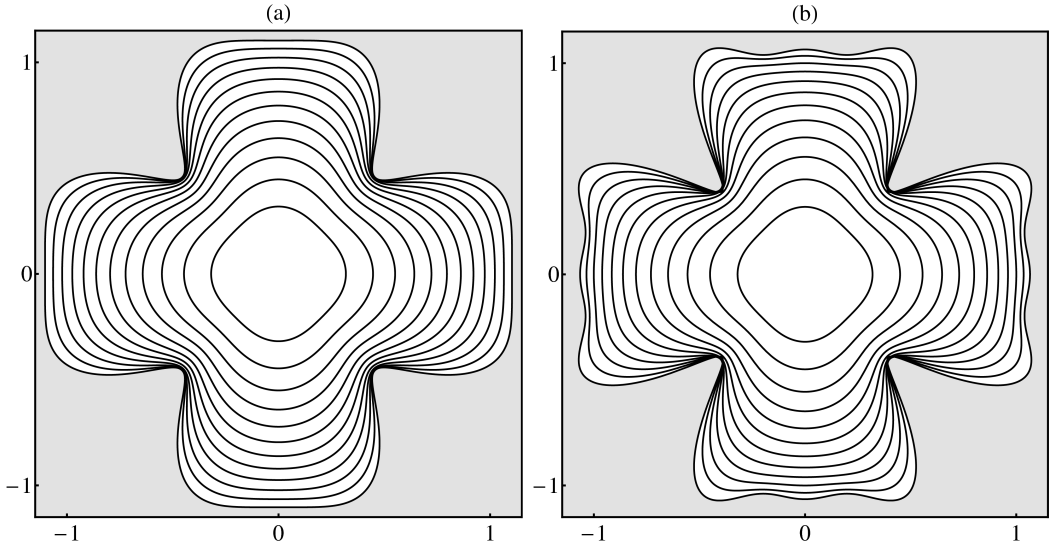

Figure 2.5 Snapshots of the evolving interface, plotted at equal time intervals for the interaction of three cosine modes $n = 4$, $2n = 8$, and $3n = 12$ when (a) $\delta = 0$, and (b) $\delta = 0.15$. Here $\Gamma = 4.45 \times 10^{-3}$, $t = t_f = 0.495$, and $R_0 = 0.1$. In (a) fingers widen and tip-splitting is imminent, while in (b) the rising of three-lobed finger shapes indicate that side branching is favored.

In Fig. 2.5(a), when yield stress effects are absent ($\delta = 0$), we see a nearly circular initial interface evolving to a four-fingered structure. Finger broadening can be observed and, at later times, the finger tips become increasingly flat, showing a tendency to bifurcate. The development of broad fingers in Fig. 2.5(a) results from nonlinear effects, as predicted by Eq. (2.47), when the mode $2n$ is driven negative. Notice that there is no sign of the presence of a mode $3n$ in Fig. 2.5(a), indicating that side branching would not be favored when $\delta = 0$.

A different scenario is observed in Fig. 2.5(b), where the yield stress parameter is nonzero ($\delta = 0.15$). Contrary to what is shown in Fig. 2.5(a), in Fig. 2.5(b) we see the development of an initially fourfold structure which evolves towards a 12-fold fingered morphology, clearly showing the presence and growth of a sizable amplitude $a_{3n} > 0$. This indicates that the presence of a nonzero, sufficiently large yield stress parameter does favor side branching formation at second order. Therefore, our weakly nonlinear results predict enhanced side branching be-

havior when the role of yield stress is taken into account.

In order to reinforce the conclusions reached from Fig. 2.5, in Fig. 2.6 we compare the time evolution of the cosine perturbation amplitudes of modes n, $2n$, and $3n$ when yield stress effects are neglected (dashed curves) and taken into account (solid curves). All initial conditions and physical parameters are identical to the ones utilized in Fig. 2.5. It is clear that as a result of the weakly nonlinear coupling we find the enhanced growth of modes $2n$ (with $a_{2n} < 0$) and $3n$ (with $a_{3n} > 0$), and a diminished growth of the fundamental mode n. This provides supplementary information supporting the effectiveness of the side branching formation mechanism at the onset of nonlinearity.

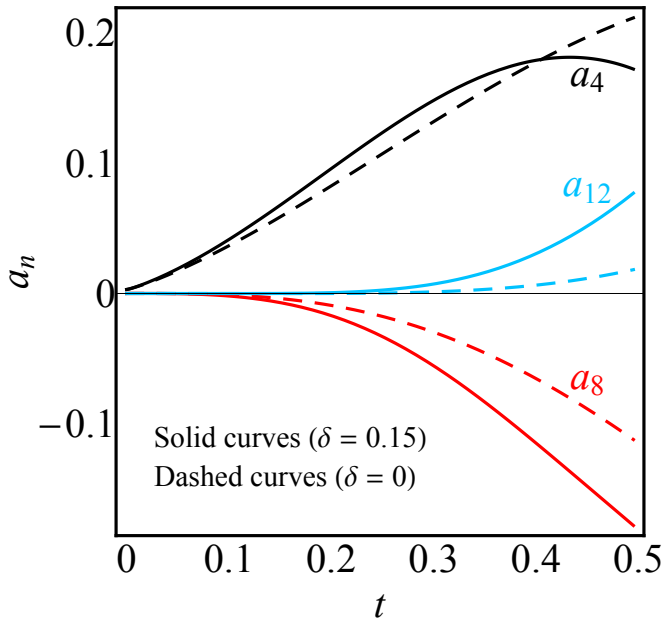

Figure 2.6 Time evolution of the cosine perturbation amplitudes of modes $n = 4$, $2n = 8$, and $3n = 12$, for $\delta = 0$ (dashed curves), and $\delta = 0.15$ (solid curves). These are the amplitudes related to the patterns depicted in Fig. 2.5.

It is worth noting that, although in Fig. 2.6 a_{2n} is more negative for the yield stress case in comparison to the Newtonian one, this does not necessarily imply that tip-splitting will be the prevalent morphological feature of the emergent pattern. As a matter of fact, the positive amplitude of a_{3n} is also increased due to the effect of the yield stress when compared to the $\delta = 0$ situation. Consequently, side branching is also favored and eventually overcomes the tip-splitting tendency. Therefore, we find necessary to plot the interface with all three modes (n,$2n$,$3n$) put together in order to determine the prevailing mechanism at the weakly nonlinear regime. As it is further discussed, we proceed by inspecting our parameter space in Fig. 2.7 to unveil the final predominant morphology for each set of parameters.

We conclude this chapter by briefly presenting a morphological "parameter diagram" for the onset of pattern formation in our radial injecting flow Hele-Shaw system with a yield stress fluid. Figure 2.7 shows typical emerging patterns by considering the parameter space (δ, Γ). Since the parameters δ [Eq. (2.7)] and Γ [Eq. (2.28)] depend on the final unperturbed radius R_f,

the representative patterns shown in the insets of Fig. 2.7 are plotted in such a way that R_f and R_0 are kept fixed, while the initial perturbation amplitudes are chosen in order to allow better visualization of the nonlinear effects. In other words, we choose the adequate perturbation amplitudes such that at $R = R_f$ the weakly nonlinear evolution reaches its limit of validity (interfaces plotted at different times do not intercept [88]). For this reason the initial conditions of the four insets of Fig. 2.7 are not exactly the same, presenting small differences in their innermost interfacial contours.

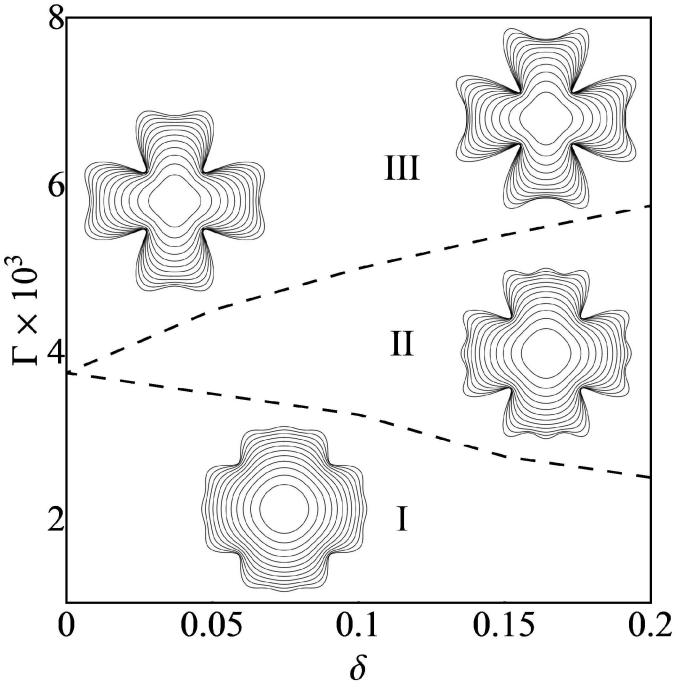

Figure 2.7 Morphological diagram in the parameter space (δ, Γ). The dashed lines delimitate the boundary between different morphological regions (I, II, and III), such boundaries were determined by examining the emerging patterns.

In the morphological diagram depicted in Fig. 2.7 we can identity three different regions: for lower values of Γ and nonzero δ(region I) we verify that tip-splitting is unfavored for a non-Newtonian yield stress fluid, so that the resulting patterns present a small bump in the middle of each evolving finger, indicating preferred side branching behavior. On the other hand, for higher values of Γ (region III) finger tip-splitting arises without any evident manifestation of side branching, generating petal-like patterns which are similar to the ones obtained in the purely Newtonian problem when δ is small. It is also clear that stronger splitting results when δ is increased, leading to shapes showing fingers with increased spreading. Finally, for intermediate values of Γ (region II) we have the delicate interplay between modes $2n$ and $3n$ mentioned earlier [Eqs. (2.49) and (2.50)], leading to a competition between the two participating mechanisms, which ends up forming three-lobed, side branched structures. We call the readers attention to the subtle difference between regions I and II, while in region I the mode $3n$ grows at the beginning of the evolution, in region II the mode $3n$ grows at the end of the evolution.

This difference is important because, in the side branching structure, the lateral branches starts to grow after the fundamental mode is fully developed. Therefore, we have the side branching structure formed in region II, while in region I it's only a seminal behavior. The morphological diagram contemplates the possibility of existence of tip-splitting events (region III), plus the prevalence of side branching phenomena (regions I and II), being generally consistent with available experimental results [47, 48].

CHAPTER 3

Lifting flow in a HSC with a yield stress fluid

3.1 Chapter outline

In this chapter we perform the weakly nonlinear analysis of the problem in which a viscous yield stress fluid, surrounded by an inviscid fluid, flows in a lifting HSC. By exploring the onset of nonlinear effects we try to gain analytical insight into the dynamic process of finger competition. Particularly, we seek to understand how mode-coupling dynamics can describe the influence of both the aspect ratio, and the non-Newtonian nature of the distended fluid on the finger competition behavior.

The remainder of this chapter is organized as follows: Sec. 3.2 presents our theoretical weakly nonlinear approach. From our modified Darcy's law for yield stress fluids [Eq. (2.6)] we derive a second-order mode-coupling equation that describes the time evolution of the interfacial amplitudes. This is done by explicitly considering the role played by the inner fluid non-Newtonian yield stress nature, as well as the geometric aspect ratio. A discussion on the action of these two elements in regulating finger competition events is presented in Sec. 3.4.

3.2 Problem formulation

Finger competition in HSC is an intrinsically nonlinear effect and cannot be properly addressed by purely linear analysis [22, 25, 49]. To elucidate key effects related to finger competition phenomena in lifting HS flow with a yield stress fluid we employ a weakly nonlinear approach. By doing this one is able to study both interface stability issues at the early linear regime, as well as important morphological aspects at weakly nonlinear, intermediate stages of pattern evolution.

We begin by considering a HS cell of a variable gap width $b(t)$ containing a non-Newtonian fluid of viscosity η and yield stress σ_0, surrounded by an inviscid Newtonian fluid [Fig. 3.1]. The surface tension between the fluids is denoted by γ. The upper cell plate can be lifted along the direction perpendicular to the plates (z-axis), and the lower plate is held fixed. The initial fluid-fluid interface is circular, having radius $R_0 = R(t=0)$ and initial gap thickness $b_0 = b(t=0)$. By using volume conservation the time dependent radius of the unperturbed interface is given by

$$R(t) = R_0\sqrt{\frac{b_0}{b(t)}}. \tag{3.1}$$

In the lifting HSC with a yield stress fluid the flow is governed by two dimensionless equa-

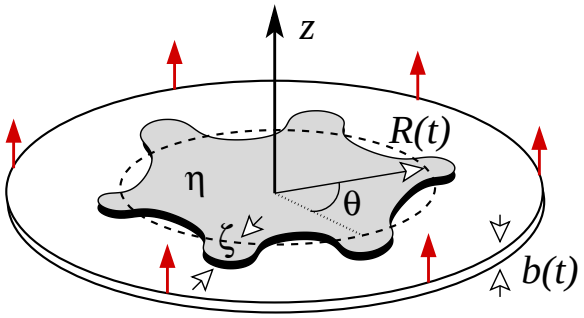

Figure 3.1 Schematic configuration of the lifting HS cell. The inner fluid (in gray) is a yield fluid of viscosity η, while the outer fluid is Newtonian and has negligible viscosity. The unperturbed time-dependent fluid-fluid interface (dashed curve) is a circle of radius $R = R(t)$. The interface perturbation amplitude is denoted by $\zeta = \zeta(\theta,t)$, and θ is the polar angle. The direction of lifting is along the z-axis.

tions: our modified Darcy's-law [Eq. (2.8)], here due to different adimensionalization,

$$\boldsymbol{\nabla} P = -\frac{q^2}{b^2}\left[1+\delta\,\frac{b}{q|\mathbf{v}|}\right]\mathbf{v}, \tag{3.2}$$

and the gap-averaged incompressibility condition [50]

$$\boldsymbol{\nabla}\cdot\mathbf{v} = -\frac{\dot{b}(t)}{b(t)}. \tag{3.3}$$

In Eq. (3.2), as in chapter 2, P is the pressure, $\mathbf{v}$ denotes the fluid velocity, and

$$q = \frac{R_0}{b_0} \tag{3.4}$$

represents the initial aspect ratio, $q \gg 1$. Its worth pointing out that $\frac{R(t)}{b(t)} \gg 1$ for all times until t_f. Moreover,

$$\delta = \frac{\sigma_0 b_0}{4\eta|\dot{b}(0)|} \tag{3.5}$$

is the yield stress parameter, similar to δ in chapter 2, that quantifies the ratio between yield stress and viscous forces, where $\dot{b}(t) = db(t)/dt$ is the upper plate velocity along the z-axis. We point out that, in Eqs. (3.2) and (3.3) in-plane lengths, $b(t)$, and time are rescaled by R_0, b_0, and the characteristic time $T = b_0/|\dot{b}(0)|$, respectively. For the rest of this work we use the dimensionless version of the equations. Here, as in chapter 2, we still interested in examining the regime where viscous forces prevail over the yield stress and flow is facilitated, which corresponds to $\delta \ll 1$.

3.3 Mode-coupling equation

To perform the weakly nonlinear analysis of the system, we consider that the initial circular fluid-fluid interface is slightly perturbed [see Fig. 3.1], $\mathfrak{R} = R(t) + \zeta(\theta,t)$ ($\zeta/R \ll 1$). As in

chapter 2, the interface perturbation is written in the form of a Fourier expansion $\zeta(\theta,t) = \sum_{n=-\infty}^{+\infty} \zeta_n(t)\exp(in\theta)$, where $\zeta_n(t) = (1/2\pi)\int_0^{2\pi} \zeta(\theta,t)\exp(-in\theta)\,\mathrm{d}\theta$ denotes the complex Fourier mode amplitudes, n is an integer wave number, and θ is the polar angle. The $n = 0$ mode is included to keep the area of the perturbed shape independent of the perturbation ζ. Mass conservation imposes that the zeroth mode is written in terms of the other modes as $\zeta_0 = -(1/2R)\sum_{n\neq 0}|\zeta_n(t)|^2$. Note that our perturbative analysis keeps terms up to the second-order in ζ and up to first order in δ.

Taking the divergence of Eq. (3.2) and using the incompressibility condition (3.3) the pressure is seen to be anharmonic (nonvanishing Laplacian). Hence, we perform our calculations considering that $\mathbf{v} = \boldsymbol{\nabla}\times\mathbf{A} - \boldsymbol{\nabla}\phi$, where

$$\phi = \frac{\dot{b}r^2}{4b} \tag{3.6}$$

is a scalar velocity potential [50, 60], and

$$\mathbf{A} \;=\; \left\{ \sum_{n\neq 0} A_n \left(\frac{r}{R}\right)^{|n|} \exp(in\theta) \;+\; \delta\left[\sum_{n\neq 0}\left(\frac{B_n}{r} + \frac{C_n}{r^3}\right)\left(\frac{r}{R}\right)^{|n|}\exp(in\theta)\right]\right\}\hat{\mathbf{z}} \tag{3.7}$$

is a vector potential. Observe that the vector potential (3.7) is simply a superposition of a purely Newtonian term ($\propto \delta^0$, coefficients A_n) and a non-Newtonian contribution ($\propto \delta^1$, coefficients B_n)

$$\mathbf{A} = \mathbf{A}_N + \mathbf{A}_{NN}. \tag{3.8}$$

The flow described by $\mathbf{A}_N$ is irrotational, while $\mathbf{A}_{NN}$ has a curl.

Similarly, we express the pressure of the inner fluid as a sum of Newtonian and non-Newtonian pressures, and propose a general form for their Fourier expansion

$$P = P_N + P_{NN}, \tag{3.9}$$

where

$$P_N = \frac{\dot{b}q^2}{4b^3}\,r^2 + \sum_{n\neq 0} p_n \left(\frac{r}{R}\right)^{|n|}\exp(in\theta), \tag{3.10}$$

and

$$\begin{aligned} P_{NN} \;&=\; -\frac{\delta q}{b}\,r \\ &+\; \delta\sum_{n\neq 0}\left(\frac{q_n}{r} + \frac{S_n}{r^3}\right)\left(\frac{r}{R}\right)^{|n|}\exp(in\theta). \end{aligned} \tag{3.11}$$

The gradient of the complex pressure field (3.9) must satisfy the non-Newtonian Darcy's law given by Eq. (3.2). By inspecting the r and θ components of (3.2), and by examining the Newtonian and non-Newtonian components of it, we can express the Fourier coefficients of P_N, P_{NN} and $\mathbf{A}_{NN}$ in terms of the Fourier coefficients of $\mathbf{A}_N$,

$$p_n = -\frac{iq^2\,\mathrm{sgn}(n)}{b^2}A_n, \tag{3.12}$$

$$q_n = -\frac{iq\beta(n)}{\dot{b}} A_n, \tag{3.13}$$

$$S_n = \frac{bq}{\dot{b}^2} \sum_{m\neq 0, m\neq n} m(n-m)\ \mu(m,n) A_m A_{n-m}, \tag{3.14}$$

$$B_n = \frac{b^2}{q\dot{b}} \alpha(n) A_n, \tag{3.15}$$

$$C_n = \frac{b^3}{q\dot{b}^2} \sum_{m\neq 0, m\neq n} im(n-m)\ \nu(m,n) A_m A_{n-m}, \tag{3.16}$$

where in order to keep the results in a more compact form, we introduced the coefficients

$$\alpha(n) = \frac{2|n|\,(|n|-1)}{(2|n|-1)}, \tag{3.17}$$

$$\beta(n) = \frac{2|n|n}{(2|n|-1)}, \tag{3.18}$$

$$\begin{aligned} \mu(n,m) &= \frac{2}{3(2|n|-3)} \Big[2n\ \mathrm{sgn}(m) \\ &+ (|n|-3)\ \mathrm{sgn}[m(n-m)] \Big], \end{aligned} \tag{3.19}$$

and

$$\nu(n,m) = \frac{1}{(|n|-3)} [n\ \mu(n,m) - 4\ \mathrm{sgn}(m)]. \tag{3.20}$$

Note that $\mathrm{sgn}(n) = 1$ if $n > 0$ and $\mathrm{sgn}(n) = -1$ if $n < 0$.

Using Eqs. (3.12)-(3.16), which are consistent with our Darcy's law (3.2), we can derive the general expression of the vector potential Fourier coefficients in terms of the perturbation amplitudes. To fulfill this goal, consider that the pressure jump condition at the interface can be written as [49, 51, 53, 55]

$$P|_{\mathfrak{R}} = \frac{\Gamma}{q}\ \kappa_{\|}|_{\mathfrak{R}}, \tag{3.21}$$

where

$$\Gamma = \frac{\gamma}{12\eta|\dot{b}(0)|}, \tag{3.22}$$

is a surface tension parameter, and $\kappa_{\|}$ is the curvature in the direction parallel to the plates.

Equation (3.21) is the simplest version of the Young-Laplace pressure boundary condition, and does not include the curvature in the direction perpendicular to the cell plates. Since the depth of the cell varies in lifting Hele-Shaw flows, in principle one could expect the perpendicular curvature to play some role on the dynamics of the system. To the best of our knowledge the only existing study which discusses the alleged role of the perpendicular curvature in lifting Hele-Shaw flows has been performed by M. Ben Amar and D. Bonn [51]. The three-dimensional model presented in Ref. [51] is somewhat involved, and just leads to a modest improved agreement between their experiments and theory. In any case, the validity and accuracy of the simpler condition given in (3.21) has been substantiated by the excellent agreement between experiments and state-of-the-art numerical simulations performed in Refs. [53,55]. In view of these facts we choose to use the simpler condition (3.21).

By expanding Eq. (3.21) up to the second-order in ζ and up to first order in δ one can find the coefficient of the vector potential corresponding to the n-th evolution mode, $A_n^{(k)}$, in terms of the k-th order in ζ (k = 1, 2) [39, 78]. These vector potential coefficients can be introduced into the kinematic boundary condition [22,49]

$$\frac{\partial \Re}{\partial t} = \left[\frac{1}{r} \frac{\partial \Re}{\partial \theta} (-v_\theta) + v_r \right]_{|\Re} , \tag{3.23}$$

which states that the normal components of each fluid's velocity at the interface equals the velocity of the interface itself. By using Eq. (3.23) plus our modified Darcy's law (3.2), and Eq. (3.21) one can finally find the equation of motion for perturbation amplitudes ζ_n. From here, the calculus and intermediate steps to the derivation of the equation of motion for perturbation amplitudes ζ_n, in this chapter, are completely analogous to those done in chapter 2. We present the evolution of the perturbation amplitudes in terms of δ and the k-th order in the perturbation amplitude ζ

$$\dot{\zeta}_n = \dot{\zeta}_n^{(1)} + \dot{\zeta}_n^{(2)}, \tag{3.24}$$

where

$$\dot{\zeta}_n^{(1)} = \lambda (n) \zeta_n, \tag{3.25}$$

$$\begin{aligned} \lambda(n) &= \frac{\dot{b}}{2b} (|n| - 1) - \frac{\Gamma b^2}{q^3 R^3} |n| \left(n^2 - 1\right) \\ &+ \delta \frac{b|n|}{(2|n| - 1) qR} \left[\frac{2\Gamma b^3}{\dot{b} q^3 R^3} |n| (n^2 - 1) - (3|n| - 1) \right], \end{aligned} \tag{3.26}$$

is the linear growth rate, and

$$\begin{aligned}\dot{\zeta}_n^{(2)} &= \sum_{m\neq n,0}\left[F_N(n,m)+\delta\ F_{NN}(n,m)\right]\ \zeta_m\zeta_{n-m}\\ &+ \sum_{m\neq n,0}\left[G_N(n,m)+\delta\ G_{NN}(n,m)\right]\ \dot{\zeta}_m\zeta_{n-m}\\ &+ \delta\sum_{m\neq n,0}H_{NN}(n,m)\ \zeta_m\dot{\zeta}_{n-m}\\ &+ \delta\sum_{m\neq n,0}J_{NN}(n,m)\ \dot{\zeta}_m\dot{\zeta}_{n-m}.\end{aligned} \tag{3.27}$$

$$F_N(n,m) = \frac{\dot{b}}{2bR}\left(n\ \mathrm{sgn}(m)-\frac{|n|}{2}-1\right)-\frac{\Gamma b^2}{q^3R^4}|n|\left(1-\frac{nm}{2}-\frac{3m^2}{2}\right), \tag{3.28}$$

$$\begin{aligned}F_{NN}(n,m) &= \frac{b}{2qR^2}\left\{\frac{f(n,m)}{2}\right.\\ &+ \left[\frac{1}{2}+\frac{2\Gamma b^3}{\dot{b}q^3R^3}\left(1-\frac{nm}{2}-\frac{3m^2}{2}\right)\right]\left[n\ \beta(n)-|n|\alpha(n)\right]\\ &+ \left.\left[|n|-1-(n-m)\frac{(2|m|-1)}{m}\right]\ \alpha(m)-\frac{|n|\beta(m)}{m}(|m|-1)\right\},\end{aligned} \tag{3.29}$$

$$G_N(n,m) = \frac{1}{R}\left[|n|\ \mathrm{sgn}(nm)-|n|-1\right], \tag{3.30}$$

$$\begin{aligned}G_{NN}(n,m) &= \frac{b^2}{\dot{b}qR^2}\left\{\frac{f(n,m)}{2}-\frac{|n|\beta(m)}{m}(|m|-1)\right.\\ &+ \left.\left[|n|-1-(n-m)\frac{(2|m|-1)}{m}\right]\alpha(m)+n\ \beta(n)-|n|\alpha(n)\right\},\end{aligned} \tag{3.31}$$

$$H_{NN}(n,m) = \frac{b^2}{2\dot{b}qR^2}f(n,m), \tag{3.32}$$

$$J_{NN}(n,m) = \frac{b^3}{\dot{b}^2qR^2}f(n,m), \tag{3.33}$$

$$f(n,m) = n\ \nu(n,m)-|n|\ \mu(n,m). \tag{3.34}$$

In Eq. (3.27) the coefficients $F_N, F_{NN}, G_N, G_{NN}, H_{NN}$, and J_{NN} represent the second-order Newtonian (N) and non-Newtonian (NN) terms. These second-order coefficients present the same special reflection symmetries described in chapter 2.

Equation (3.24) is the mode-coupling equation of the lifting HSC problem with a yield stress fluid. It gives us the time evolution of the perturbation amplitudes ζ_n, accurate to second-order, in the weak yield stress limit. Notice that Eq. (3.24) is conveniently written in terms of three dimensionless quantities: the aspect ratio q [Eq. (3.4)], the yield stress parameter δ [Eq. (3.5)], and the surface tension parameter Γ [Eq. (3.22)]. Since the role of Γ has already been sufficiently discussed in Refs. [50, 53, 55], we focus on understanding the action of q and δ in determining stability and shape of the interface.

Despite the complex functional form of the mode-coupling terms in (3.27), as we will see in Sec. 3.4.2 the weakly nonlinear scheme furnishes a fairly simple picture for the important mechanism of finger competition in lifting HS flows. It should be noted that the theoretical results presented in the following sections utilize dimensionless quantities which are extracted from the realistic physical parameters used in the experiments of Refs. [52, 53, 55]. In accordance with these experimental studies we consider that the gap width grows linearly with time, so that the lifting velocity $\dot{b}$ is constant.

3.4 Discussion

We proceed by using our mode-coupling approach to investigate the interface evolution at first and second order in ζ. To simplify our discussion it is convenient to rewrite the net perturbation (2.10) in terms of cosine and sine modes, as we did in chapter 2 [Eq. (2.44)].

Without loss of generality, for the remainder of this chapter, we choose the phase of the fundamental mode so that $a_n > 0$ and $b_n = 0$. Henceforth, we study the development of interfacial instabilities, and examine how the yield stress parameter δ and the aspect ratio q affect the finger competition dynamics.

3.4.1 First order: Linear analysis

Before analyzing the weakly nonlinear regime, and try to understand how nonlinearity affects the finger competition, we briefly discuss some useful information which can be extracted from the linear growth rate (3.26). We start by discussing the physical origin of each term in the linear growth rate expression. Since a positive growth rate $\lambda(n)$ leads to an unstable interface, Eq. (3.26) tells us that the lifting force contribution appearing as the first term on the right hand side tends to destabilize the system since $\dot{b} > 0$. On the other hand, the second term proportional to $|n|(n^2-1)$ is associated to the surface tension connected to the in-plane curvature, and plays a stabilizing role. It can be noticed that increasingly larger values of q (large confinement) tend to inhibit the stabilizing effect due to surface tension.

The description of the terms proportional to δ in Eq. (3.26) is as follows: the first contribution is due to the coupling between the surface tension parameter Γ and yield stress, and its net effect is destabilizing. Meanwhile, the second term is uniquely related to yield stress and has a stabilizing role. We have verified that for the typical experimental circumstances of

Refs. [52, 53, 55] this last term is dominant so that the overall linear effect of the term proportional to δ in Eq. (3.26) is indeed to stabilize the interface. We can also see that strong confinement (high aspect ratio) leads to a less efficient stabilization via yield stress effects.

We continue by briefly discussing some useful information which can be extracted from the linear growth rate (3.26). The wave number of maximum growth [obtained by setting $d\lambda(n)/dt = 0$] for a Newtonian fluid ($\delta = 0$) can be easily calculated from Eq. (3.26), yielding

$$n_{max}^N = \sqrt{\frac{1}{3}\left(1 + \frac{q^3 R^3 \dot{b}}{2b^3\Gamma}\right)}. \tag{3.35}$$

From Eq. (3.26), one can obtain an explicit solution for the wave number n_{max} with maximal growth rate for a yield stress fluid ($\delta \neq 0$). Although this expression is rather complex, in the limit $(n_{max}^N)^2 \gg n_{max}^N \gg 1$ (which is consistent with experiments [52, 53, 55]) it simplifies to

$$n_{max} \approx n_{max}^N \left(1 - \delta \frac{b^2}{\dot{b} q R}\right), \tag{3.36}$$

the intermediate steps to this calculus are analogous to those in appendix A. One can verify that the critical wave number [obtained by setting $\lambda(n) = 0$] which is the maximum wave number for which the growth rate is still positive, is slightly shifted towards lower wave numbers as the yield stress parameter δ is increased. We can also verify in Eqs. (3.26) and (3.36) that when q is too large (great confinement) the yield stress contribution tends to decay so the behavior of the non-Newtonian fluid approaches the Newtonian one.

In opposition to Fig. 2.2, Fig. 3.2 shows us that, in the lifting-driven flow, the effect of δ at linear level is very slight. On the other hand, in Fig. 3.2 we can see that the effect of the aspect ratio at linear level is very strong.

From the findings presented in this section we see that yield stress effects tend to stabilize the interface in the weak yield stress regime. Since n_{max} [Eq. (3.36)] is related to the typical number of fingers formed at the onset of the instability, this means that higher δ would induce the formation of patterns tending to present a decreased number of fingered structures. Conversely, larger q tend to destabilize the system favoring the development of patterns having more fingers.

3.4.2 Second order: Weakly nonlinear analysis

Now the full mode-coupling equation (3.24) is utilized to study the onset of pattern formation through the coupling of a small number of modes. We follow Refs. [25, 60] and consider finger length variability as a measure of the competition among fingers. Within our approach the finger competition mechanism can be described by the influence of a fundamental mode n, assuming n is even, on the growth of its sub-harmonic mode $n/2$. By using Eqs. (3.24)-(3.27) the equations of motion for the sub-harmonic mode can be written as

$$\dot{a}_{n/2} = \{\lambda(n/2) + \mathcal{C}(n)\, a_n\}\; a_{n/2}, \tag{3.37}$$

$$\dot{b}_{n/2} = \{\lambda(n/2) - \mathcal{C}(n)\, a_n\}\; b_{n/2}, \tag{3.38}$$

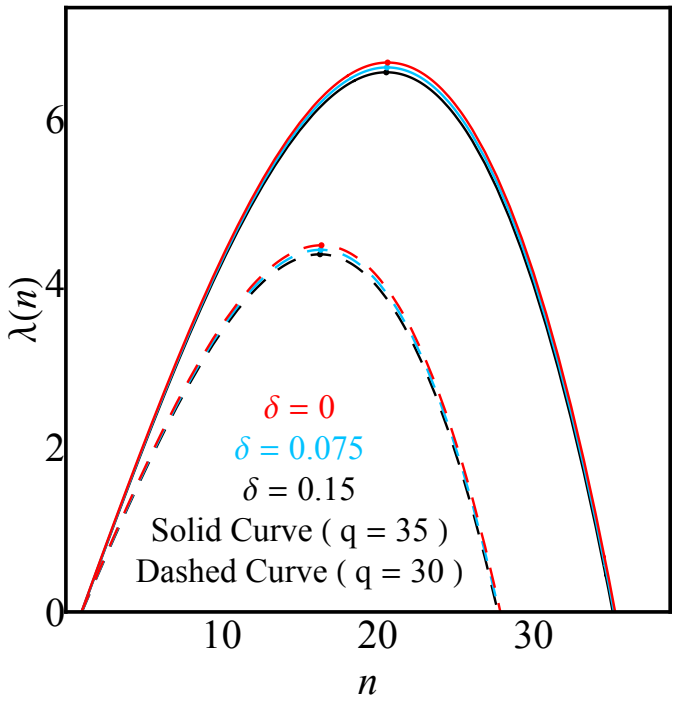

Figure 3.2 Linear growth rate $\lambda(n)$ as a function of mode n, for three values of δ and two values of q, surface tension parameter $\Gamma = 0.5$, and $t = t_f = 0.0015$. To better guide the eye the maxima of the curves are explicitly indicated by small dots.

where the finger competition function is given by

$$\mathcal{C}(n) = \frac{1}{2}\left[T\left(\frac{n}{2},-\frac{n}{2}\right) + T\left(\frac{n}{2},n\right)\right], \tag{3.39}$$

and $T(n,m)$ is described in Eq. (2.48).

From Eqs. (3.37) and (3.38) we verify that a negative $\mathcal{C}(n)$ increases the growth of the sine sub-harmonic $b_{n/2}$, while inhibiting growth of its cosine sub-harmonic $a_{n/2}$. The result is an increased variability among the lengths of fingers of the outer fluid penetrating into the inner one. This effect describes the competition of inward fingers. We stress this is in line with what is observed in numerical simulations [50] and experiments [52, 53, 56]. Reversing the sign of $\mathcal{C}(n)$ would exactly reverse these conclusions, such that modes $a_{n/2}$ would be favored over modes $b_{n/2}$. In this case, competition of the outward moving fingers of the inner fluid would have preferential growth.

At this point we emphasize a few important ideas related to the finger competition mechanism described by Eqs. (3.37) and (3.38). The action of the sub-harmonic mode breaks the n-fold rotational symmetry of the fundamental by alternately increasing and decreasing the length of each of the n fingers. The fact that when $\mathcal{C}(n) < 0$ sine modes $b_{n/2}$ grow, and cosine modes $a_{n/2}$ decay does not really mean that finger competition only occurs for inward moving fingers. Actually, finger competition is present for both inward and outward moving fingers. However, while the competition among inward moving fingers is favored, the competition among outward moving fingers is restrained. What our finger competition mechanism

determines is the preferred direction for finger growth and finger length variability. So, when $\mathcal{C}(n) < 0$, even though there exists finger competition in both directions (inward and outward), the competition among inward moving fingers is much stronger than the competition among outward moving fingers.

For the typical experimental parameters used in Refs. [52, 53, 55] we have found that $\mathcal{C}(n) < 0$ indicating a restrained growth of cosine sub-harmonic modes $a_{n/2}$, accompanied by a simultaneous increased growth of sine sub-harmonic modes $b_{n/2}$. This general behavior is illustrated in Fig. 3.3 which depicts the time evolution of the mode amplitudes (a) $a_{n/2}$, and (b) $b_{n/2}$ for different values of the yield stress parameter δ, and aspect ratio q. In Fig. 3.3 we take the initial amplitudes as $a_{n/2}(0) = b_{n/2}(0) = 0.001$, and $a_n(0) = 0.01$. In addition, $\Gamma = 0.5$, and the final time $t_f = 0.0015$. These parameters are also utilized to plot Fig. 3.4 and Fig. 3.5.

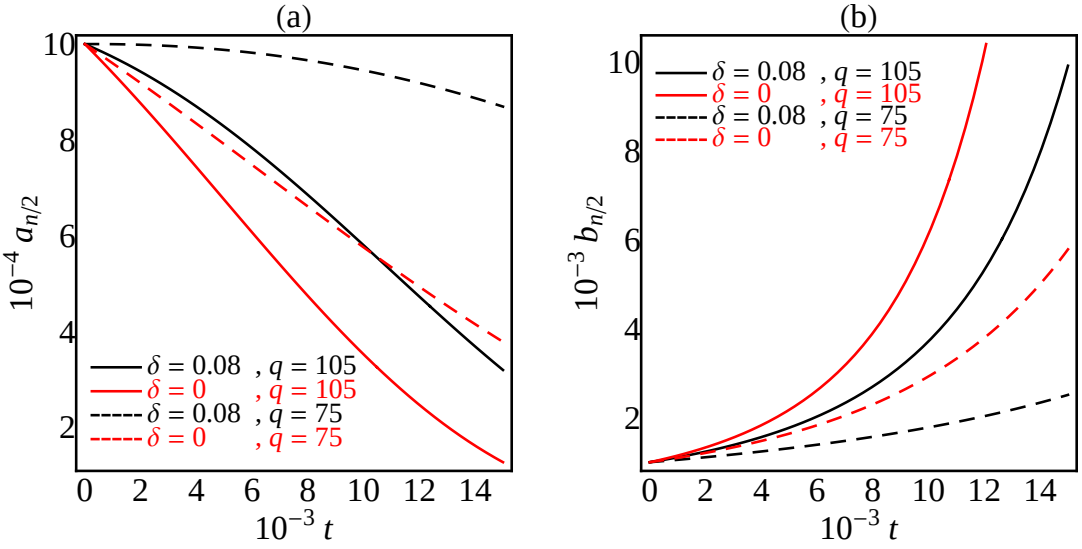

Figure 3.3 Time evolution of the (a) cosine ($a_{n/2}$) and (b) sine ($b_{n/2}$) perturbation amplitudes for the sub-harmonic mode, considering different values of δ and q. Here $a_{n/2}(0) = b_{n/2}(0) = 0.001$, $a_n(0) = 0.01$, $\Gamma = 0.5$, and $t_f = 0.0015$.

In Fig. 3.3 curves in black (gray) show the amplitudes' time evolution when the inner fluid is yield stress (Newtonian). Moreover, the solid (dashed) curves depict the situation in which the aspect ratio is large (small), given by $q = 105$ ($q = 75$). By inspecting Fig. 3.3(a) it is clear that the amplitudes of the mode $a_{n/2}$ do tend to decrease as time progresses. Regardless the value of the aspect ratio q one observes that the yield stress nature of the inner fluid tend to attenuate such a decrease. It is also evident that stronger attenuation takes place for large values of q. On the other hand, by examining Fig. 3.3(b) we notice that the amplitudes of the sine mode $b_{n/2}$ show an increase as time evolves. But, similarly to what has been seen in Fig. 3.3(a) the growth of $b_{n/2}$ is unfavored for larger (smaller) values of δ (q). Therefore, the main conclusion extracted from Fig. 3.3 is that finger competition of inward moving fingers is facilitated for stronger confinement (i.e. larger q), and inhibited for higher yield stress effects (larger δ).

In Fig. 3.3 we can also verify that the difference between yield stress and Newtonian curves is smaller for low values of q, this is in agreement with Eqs. (3.26) and (3.36) where we can see that greater confinement (large q) tends to decrease the difference between Newtonian and yield stress behavior.

In order to reinforce the conclusions reached from Fig. 3.3, and to illustrate our finger competition findings in a more pictorial way in Fig. 3.4 we plot the fluid-fluid interface at final time $t = t_f = 0.0015$ as a function of the polar angle θ. Recall that here we consider the same initial conditions and physical parameters used in Fig. 3.3. This is done for different values of δ and q. The most noteworthy feature of Fig. 3.4 is the conspicuous competition between the inward moving fingers of the outer fluid penetrating the inner fluid. It is also clear that the outward moving fingers of the inner fluid do not tend to compete as much. All these more visual verifications are in agreement with the predictions based on the mode-coupling equations (3.37) and (3.38), and with the fact that the finger competition function $\mathcal{C}(n)$ is negative. By examining Fig. 3.4 we can also confirm the fact the finger competition of inward moving fingers is enhanced for larger values of the aspect ratio, and repressed by yield stress effects.

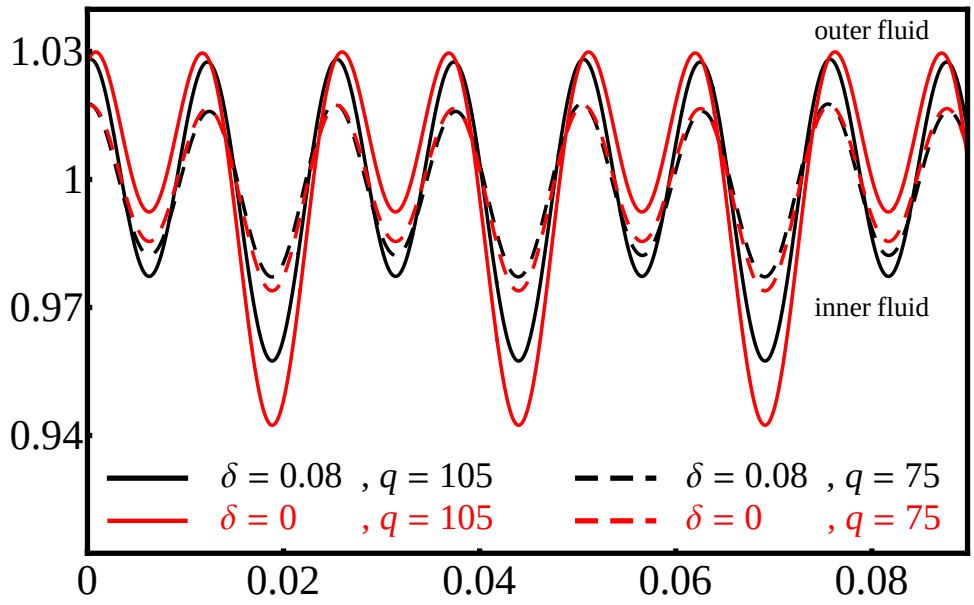

Figure 3.4 Snapshot of the fluid-fluid interface position $\mathfrak{R}$ as a function of the polar angle θ at $t = t_f = 0.0015$, for different values of δ and q. This graph uses the same physical parameters utilized in Fig. 3.3.

Complementary information about the time evolution of the finger competition behavior in our system can be obtained by analyzing Fig. 3.5 that plots the difference in finger lengths for consecutive inward moving fingers $\Delta\mathfrak{R}$ as a function of time, for $0 \leq t \leq t_f$. Note that the quantity $\Delta\mathfrak{R}$ is obtained by calculating the difference between the interface positions of the finger tips $\mathfrak{R}$ for consecutive inward moving fingers of the outer fluid. Finger length variability (i.e. finger competition) does not change much if q and δ are varied at lower times. However, as time advances we can easily verify that finger competition of inward fingers does increase

significantly for higher values of q, and tends to be diminished by the action of yield stress effects.

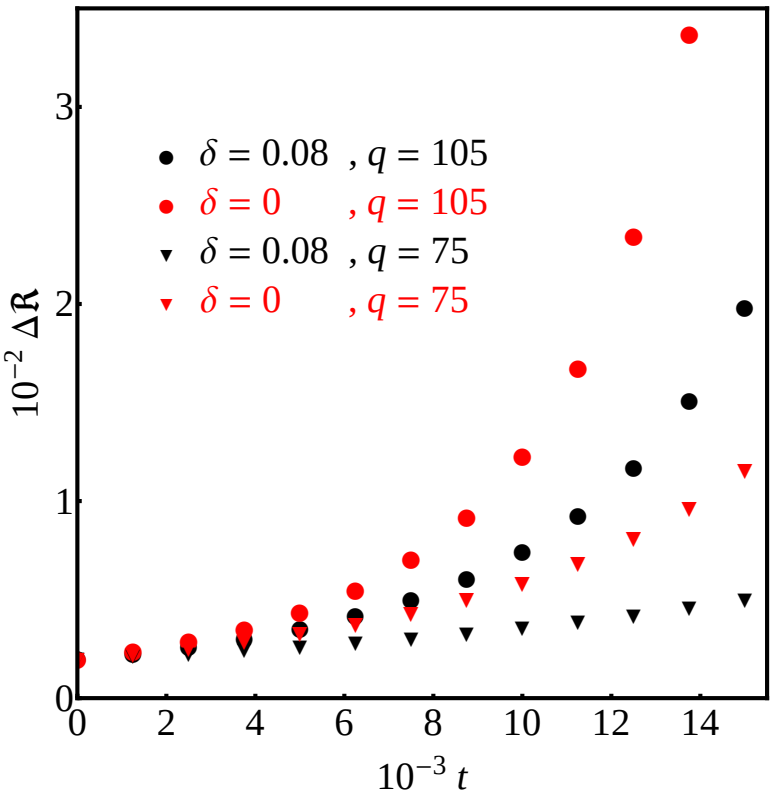

Figure 3.5 Difference between the interface positions of the finger tips for consecutive inward moving fingers of the outer fluid $\Delta\mathfrak{R}$ as a function of time, for different values of δ and q. This figure uses the same physical parameters utilized in Figs. 3.3 and 3.4.

CHAPTER 4

Controlling and minimizing fingering instabilities in non-Newtonian power-law fluids in a injection-driven HSC

4.1 Chapter outline

In this chapter, differently of the previous ones, we study the linear analysis of the problem in which a non-Newtonian fluid flows, in a radial HSC, being pushed by an injected Newtonian fluid. By exploring the onset of linear effects we try to understand the dynamic process of controlling and minimizing fingering formation. As in Ref. [41] we study a situation in which the dislocated fluid exhibits the simplest non-Newtonian rheology: a power-law viscosity. In this framing, we focus on examining how the existing stabilization protocols for Newtonian fluids [26, 66–77] are modified by the fact that the displaced fluid can be either shear-thinning or shear-thickening.

The rest of this chapter is organized as follows: Sec. 4.2 formulates the problem and derives the growth rate for the power-law fluids. In Sec. 4.3 we expose the variational strategy for minimizing fingering instabilities. Finally, in Sec. 4.4 we present our strategy to control the number of fingers at the interface.

4.2 Problem formulation and linear growth rate

Consider the displacement of a viscous, non-Newtonian, power-law fluid by a Newtonian fluid of negligible viscosity in a quasi-two-dimensional Hele-Shaw cell of constant gap spacing b. We define a cylindrical coordinate system (r,θ,z) in such a way that its origin is located at the center of the cell. The lower (upper) Hele-Shaw cell plate is located at $z=0$ ($z=b$), and the surface tension between the fluids is denoted by σ. Note that b is the smallest length scale of the problem. The inviscid fluid is injected into the non-Newtonian fluid through a role localized at the origin, at a given injection rate $Q=Q(t)$ (equal to the area covered per unit time) which may depend on time.

The perturbed fluid-fluid interface [see Fig. 4.1] is described as $\mathscr{R}(\theta,t)=R(t)+\zeta(\theta,t)$ ($\zeta/R\ll 1$), where θ represents the azimuthal angle, and $R(t)$ is the time dependent unperturbed radius

$$R(t)=\sqrt{R_0^2+\frac{1}{\pi}\int_0^t Q(t')dt'}, \tag{4.1}$$

with R_0 being the unperturbed radius at $t=0$. The interface perturbation is written in the form

of a Fourier expansion [Eq. 2.10].

The perturbative approach we employ keeps terms up to the first-order in ζ. Our main task in this section is to obtain the linear growth rate of interfacial perturbations. This is a lengthy and nontrivial calculation that has been originally performed by Sader et al. [41]. For the sake of clarity below we describe the main steps of the derivation. We refer the reader to Ref. [41] for details. It is worth pointing out that the linear growth rate plays a central role in the controlling and minimizing schemes that will be described and discussed in Sec. 4.3 and 4.4.

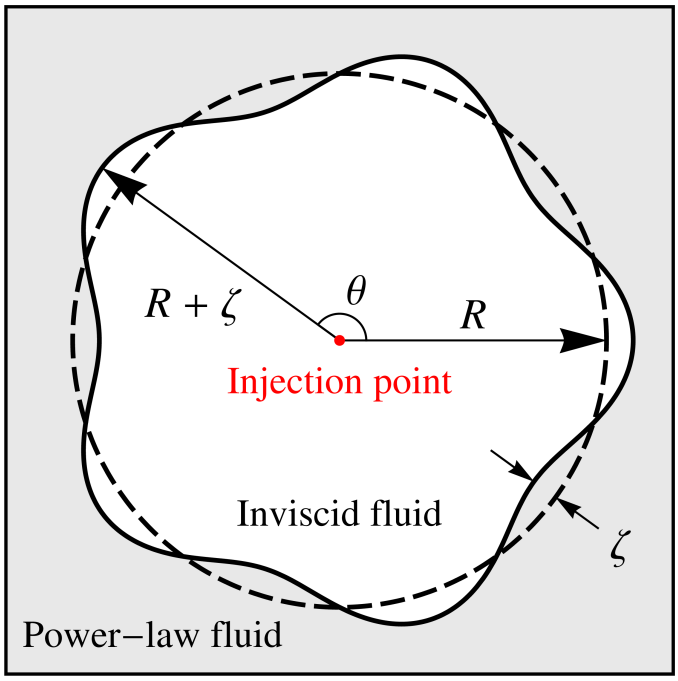

Figure 4.1 Schematic illustration (top view) of the radial flow in a Hele-Shaw cell. The inner fluid is inviscid and the outer fluid is a power-law fluid. The unperturbed time-dependent fluid-fluid interface (dashed curve) is a circle of radius $R = R(t)$. The interface perturbation amplitude is denoted by $\zeta = \zeta(\theta,t)$, and θ is the azimuthal angle. The injection point is located at the center of the cell.

The non-Newtonian fluid with which we will be concerned is described by the Oswald-de Waele power-law model [27, 41, 79, 91] whose constitutive equation is

$$\boldsymbol{\tau} = 2m[2\mathbf{e} : \mathbf{e}]^{(\alpha-1)/2}\mathbf{e}, \tag{4.2}$$

where $\boldsymbol{\tau}$ is the excess stress tensor, $\mathbf{e} = [\boldsymbol{\nabla}\mathbf{u} + (\boldsymbol{\nabla}\mathbf{u})^T]/2$ is the rate-of-strain tensor, with $\mathbf{u}$ being the three-dimensional velocity vector, $(\boldsymbol{\nabla}\mathbf{u})_{ij} = \partial_i u_j$, and T denotes matrix transposition. Note that in Eq. (4.2) the colon represents an inner product, $\mathbf{e} : \mathbf{e} = \sum_{k,l} \mathrm{e}_{kl}\mathrm{e}_{lk}$ where e_{kl} are the Cartesian components of tensor $\mathbf{e}$. In addition, m and α are positive material constants. The constant α ($0 < \alpha < 2$) is the so-called power-law index, with $\alpha < 1$ corresponding to a shear-thinning fluid, $\alpha > 1$ to a shear-thickening fluid, and $\alpha = 1$ to a Newtonian fluid. The constant m relates the Newtonian viscosity to the power-law index α.

Ignoring inertia and body forces the governing equations of the system are the Navier-Stokes equation

$$\boldsymbol{\nabla}\cdot\boldsymbol{\tau}=\boldsymbol{\nabla}P, \tag{4.3}$$

and the continuity equation for an incompressible fluid

$$\boldsymbol{\nabla}\cdot\mathbf{u}=0, \tag{4.4}$$

where $P=P(r,\theta,z)$ is the pressure. In the framework of the quasi-two-dimensional geometry of the Hele-Shaw cell, the problem is specified by two boundary conditions [2, 49]: (i) the pressure jump boundary condition

$$p|_{r=\mathscr{R}}=-\sigma\kappa|_{r=\mathscr{R}}, \tag{4.5}$$

where $p(r,\theta)=\int_0^b P(r,\theta,z)dz/b$ is the gap-averaged pressure, and κ is the interfacial curvature κ in the plane of the Hele-Shaw cell; plus (ii) the kinematic boundary condition

$$\frac{\partial\mathscr{R}}{\partial t}=\left(v_r-\frac{1}{r}\frac{\partial\mathscr{R}}{\partial\theta}v_\theta\right)_{r=\mathscr{R}}, \tag{4.6}$$

which states that the normal components of each fluid's velocity at the interface is equal to the velocity of the interface itself. Here $\mathbf{v}(r,\theta)=(v_r,v_\theta)=\int_0^b\mathbf{u}(r,\theta,z)dz/b$ represents the two-dimensional gap-averaged fluid velocity. Note that within the scope of the linear stability theory Eq. (4.5) relates p with ζ_n and σ, while Eq. (4.6) connects the interface velocity components with both ζ_n and $\dot{\zeta}_n$.

To obtain the equation of motion for the perturbation amplitude ζ_n, first one applies a first-order perturbation method to the constitutive Eq. (4.2) and to the governing Eqs. (4.3) and (4.4), imposing the no-slip boundary conditions at the cell's plates, i.e. $\mathbf{u}=0$ at $z=0$ and $z=b$. Then, upon consideration of the pressure interface condition (4.5) and the kinematic boundary condition (4.6), one obtains that

$$\dot{\zeta}_n=\lambda(n)\zeta_n, \tag{4.7}$$

where the overdot means total time derivative,

$$\lambda(n)=\frac{\dot{R}}{R}\left[\frac{n^2}{c(n)}-1\right]-\Gamma(\alpha)\frac{\dot{R}^{(\alpha-1)}}{R^{(5-2\alpha)}}\left[\frac{n^2(n^2-1)}{c(n)}\right], \tag{4.8}$$

is the linear growth rate, $\dot{R}=Q/(2\pi R)$,

$$c(n)=\frac{1-\alpha+\sqrt{(1-\alpha)^2+4n^2\alpha}}{2}, \tag{4.9}$$

and

$$\Gamma(\alpha)=\left[\frac{4-c(2)}{12}\right]\left(\frac{\sigma b^2}{2\eta}\right)^{(2-\alpha)}. \tag{4.10}$$

In Eq. (4.10) η is the viscosity of the fluid when $\alpha = 1$. Equation (4.8) reproduces the classic linear dispersion relation derived by Paterson [see Eq. (10) in Ref. [22]] for radial Hele-Shaw flow with Newtonian fluids when one sets $\alpha = 1$. The solution of the Eq. (4.7) is given by

$$\zeta_n(t) = \zeta_n(0)\exp\{I(n,R,\dot{R})\}, \tag{4.11}$$

where

$$I(n,R,\dot{R}) = \int_{t_c(n)}^{t} \lambda(n,R,\dot{R})dt', \tag{4.12}$$

with $t_c(n)$ being the time at which a mode n becomes unstable [$\lambda(n) = 0$], and $\lambda(n) = \lambda(n,R,\dot{R})$. We assume that $\zeta_n(t) = \zeta_n(0)$ if $0 \leq t < t_c(n)$ [25,71]. We point out that the theoretical results presented in this chapter are obtained by utilizing parameter values that are consistent with those used in typical experimental realizations of radial Hele-Shaw flows with Newtonian [22–24, 26, 66, 67] and non-Newtonian [28–31] fluids: $\eta = 8$ g/(cm s), $\sigma = 25$ dyne/cm, $b = 0.1$ cm, and $R_0 = 0.45$ cm.

We close this section by adding a brief discussion of the validity of the linearization about the time-varying base state. In general, when linear stability analyses are performed about a non-stationary frame of reference it is known that so-called Perron effects [89] may invalidate the usual approach to the stability of the problem. For instance, finding negative eigenvalues of the linearized evolution operator does not generally mean stability of the underlying time-dependent solution. The converse is also true: finding positive eigenvalues does not generally mean instability. However, we point out that when Eq. (4.7) is written in matrix form for modes n, we end up with a linear system of decoupled equations, where the matrix associated to the system is already diagonal. In this case the base of eigenvectors [the modes $\exp(in\theta)$] is time-independent so that the information about the stability of the system can be reliably extracted from the eigenvalues $\lambda(n)$. Under such circumstances, Perron-type difficulties can be excluded. On the other hand, whenever such difficulties arise one could use a “quasi-steady" strategy [90], and consider that the time scale of any disturbances is implicitly assumed to be much faster than the time scale on which the base state changes. In this framework, Perron-type difficulties can be properly avoided.

4.3 Minimizing the interfacial amplitudes

A variational method aimed to minimize interfacial instabilities occurring between two immiscible Newtonian fluids in a Hele-Shaw cell has been recently proposed in Ref. [71]. This controlling technique has been successfully applied for the injection-driven flow in a radial Hele-Shaw cell in the following context: if one wishes to inject a certain volume of fluid in a given time, what would be the optimal time-dependent injection rate $Q(t)$ so that the emerging perturbation amplitudes could be minimized? In this section, we apply this approach and answer this arduous question to an even more complex situation involving the radial Hele-Shaw flow of an inviscid fluid displacing a viscous, non-Newtonian, power-law fluid.

At the linear level, the mode of maximum growth rate ($n_{\max}$) can be obtained by the condi-

tion $[\mathrm{d}\lambda(n)/\mathrm{d}n]_{n=n_{\max}} = 0$. This calculation yields

$$n_{\max} = \sqrt{\frac{1}{3}\left[1+\frac{(R^2\dot{R})^{2-\alpha}}{\Gamma(\alpha)}\right]} \approx \sqrt{\frac{(R^2\dot{R})^{2-\alpha}}{3\Gamma(\alpha)}} \tag{4.13}$$

for an unstable growth situation of the interface. Notice that we can minimize the perturbations amplitudes (4.11) by extremizing the integral (4.12). Moreover, since $n_{\max}$ is the fastest growing mode, we focus on minimizing the integral

$$I(n_{\max}, R, \dot{R}) = \int_0^t \lambda(R,\dot{R})dt', \tag{4.14}$$

where $t_c(n_{\max}) = 0$ and

$$\lambda(R,\dot{R}) \approx \frac{2}{3}\frac{1}{\sqrt{3\alpha\Gamma(\alpha)}}\frac{\dot{R}^{2-\alpha/2}}{R^{\alpha-1}} - \frac{\dot{R}}{R} \tag{4.15}$$

only depends on R and $\dot{R}$. This simplified growth rate expression is obtained by using Eq. (4.8), Eq. (4.13), and taking $c(n) \approx n\sqrt{\alpha}$. We have verified that the convenient approximation $c(n) \approx n\sqrt{\alpha}$ involves an error smaller than 5 % to $n_{\max}$, if $0 < \alpha < 1.8$. Therefore, in practical terms it can be utilized without loss of accuracy. This assumption will be used in the remainder of this chapter, and is a key point to allow analytical access to our major findings.

In the minimization process of Eq. (4.14) we wish to inject a certain amount of the inviscid fluid by keeping fixed initial and final radii, during a time interval $[0, t_f]$. Under such circumstances, we have a variational problem which can be solved by using the Euler-Lagrange equation

$$\frac{d}{dt}\left(\frac{\partial\lambda}{\partial\dot{R}}\right) = \frac{\partial\lambda}{\partial R}, \tag{4.16}$$

with fixed endpoints $R(t=0) = R_0$ and $R(t=t_f) = R_f$. Substituting the growth rate (4.15) into Eq. (4.16) we obtain the differential equation

$$\ddot{R} = \frac{2(\alpha-1)}{(4-\alpha)}\frac{\dot{R}^2}{R}, \tag{4.17}$$

whose solution can be neatly written as

$$R(t) = \left[R_0^\gamma + \frac{(R_f^\gamma - R_0^\gamma)}{t_f}\,t\right]^{1/\gamma}, \tag{4.18}$$

where

$$\gamma = \frac{3(2-\alpha)}{(4-\alpha)}, \tag{4.19}$$

see table (4.1).

From Eq. (4.1) $Q(t) = 2\pi R\dot{R}$, then it's possible o write the optimal pumping rate as

$$Q(t) = 2\pi\frac{(R_f^\gamma - R_0^\gamma)}{\gamma\, t_f}\left[R_0^\gamma + \frac{(R_f^\gamma - R_0^\gamma)}{t_f}\,t\right]^{(2-\gamma)/\gamma}. \tag{4.20}$$

α	γ	$\frac{2-\gamma}{\gamma}$	$\frac{1}{2-\alpha}$
0	$\frac{3}{2}$	$\frac{1}{3}$	$\frac{1}{2}$
1	1	1	1
2	0	∞	∞

Table 4.1 Table showing the values of the exponents according to the power-law index α.

It is interesting to note that our optimal pumping rate (4.20) does not depend either on the Hele-Shaw cell gap width b or on the material properties of the fluids (η and σ). However, there is a clear dependence on the power-law index α [see Fig 4.2]. Notice that when $\alpha = 1$ ($\gamma = 1$) Eq. (4.20) reproduces the simpler Newtonian result originally obtained in Ref. [71] where the optimum injection rate evolves linearly with time.

Before we proceed an important clarification must be given: despite its simplicity and elegance, the minimization procedure described above leading to Eq. (4.20) does not provide a rigorous mathematical proof that it really provides the true optimum minimum of the problem. Note that our main approximation is that we minimize the integral $I(n_{\max}, R, \dot{R})$ [see Eq. (4.14), where $n = n_{\max}$], and not the maximum of $I(n, R, \dot{R})$ with respect to $R(\{n\}, t)$, which is a much more difficult task. On the other hand, the validity of our simplified theoretical minimization procedure has been substantiated by laboratory experiments and fully nonlinear numerical simulations in Ref. [71] for the Newtonian flow case. These facts support the idea that despite of the fact that our minimization procedure may not lead to the exact true optimum of the problem, it does offer a useful and simple approximation to it. So, in this chapter whenever we mention the optimal (or, ideal) injection rate we refer to it in the context of our simplified minimization method.

Usual radial viscous fingering flow considers insertion of a specific volume of fluid at a constant injection rate. Under such circumstance, with $R(t = 0) = R_0$ and $R(t = t_f) = R_f$, Eq. (4.1) can be written as

$$Q_0 = \frac{\pi(R_f^2 - R_0^2)}{t_f}. \tag{4.21}$$

Notice that from Eq. (4.21) the parameters to be fixed in the variational protocol could be either R_f and t_f, or Q_0 and t_f. Figure 4.2 depicts how the optimum injection rate $Q(t)$ [Eq. (4.20)] varies with time when the displaced fluid is Newtonian ($\alpha = 1$), shear-thinning ($\alpha = 0.6$), and

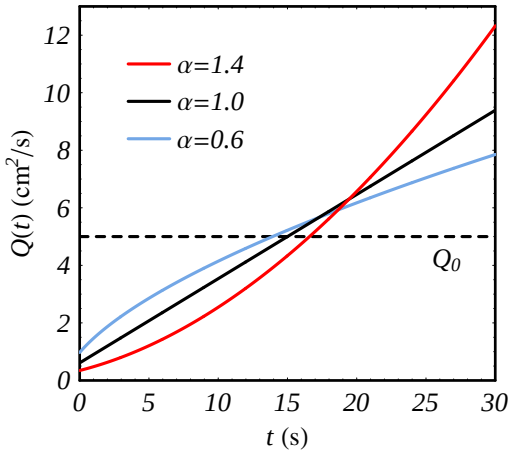

Figure 4.2 Time-dependent injection rate as a function of time for the optimal injection $Q(t)$ (solid curves) and the equivalent constant injection rate Q_0 (dashed line). Here we set $\alpha = 1.4$, $\alpha = 1.0$, and $\alpha = 0.6$. The total volume of injected fluid (area under the curves) in the interval $[0, t_f]$ should be the same for all pumping rates.

shear-thickening ($\alpha = 1.4$). The dashed horizontal line represents the equivalent constant injection rate Q_0 [Eq. (4.21)]. Here we set $Q_0 = 5$ cm^2/s, and $t_f = 30$ s. One can see that the volume of injected fluid is the same for all pumping rates but just at $t = t_f$, before and after that $R(t)$ is different for each pumping rate. It is worth noticing that when the displaced fluid is shear-thinning (shear-thickening) in order to minimize interfacial disturbances one should first inject with an injection rate higher (lower) than the one used in the Newtonian case. Then, for later times the opposite situation must take place to ensure amplitude minimization: lower (higher) pumping rate as compared with the Newtonian case, if the dislocated fluid is shear-thinning (shear-thickening).

Now we turn to the comparison of the resulting interface morphologies obtained when ones utilizes the constant injection rate (4.21), and the ideal pumping rate (4.20) at $t = t_f$. The results presented in Fig. 4.3 are obtained by setting the initial perturbation amplitude $10^{-4}R_0$, and final time $t_f = 27$ s. Figure 4.3 plots the amplitude given by Eq. (4.11) divided by the unperturbed radius at t_f, for the optimal pumping $\zeta_n(t_f)/R_f$ (solid curves), and for the equivalent constant injection $\zeta_n^0(t_f)/R_f$ (dashed curves) as functions of the wave number n. The constant injection rate Q_0 and α are: (a) 11.1 cm^2/s and 1.4; (b) 2.26 cm^2/s and 1.0; (c) 1.0 cm^2/s and 0.6. Note that the values of Q_0 were chosen so that $\zeta_n^0(t_f)/R_f$ has approximately the same magnitude ($\approx$ 0.08). This procedure allows us to compare the efficacy of the variational method for different power law indices α.

By examining Fig. 4.3, we can readily see a substantial reduction of the final perturbation amplitudes when the ideal injection is used. Furthermore, it is also observed that the stabilization protocol works better for the shear-thickening case [Fig. 4.3(a)]. The physical explanation for the success of the optimum stabilization method [Eq. (4.20)] is based on the fact that initially $Q(t)$ is sufficiently small, so that the front evolves with a sizable unperturbed shape. As time progresses the pumping increases appreciably, but as long as it takes place at a large interfacial

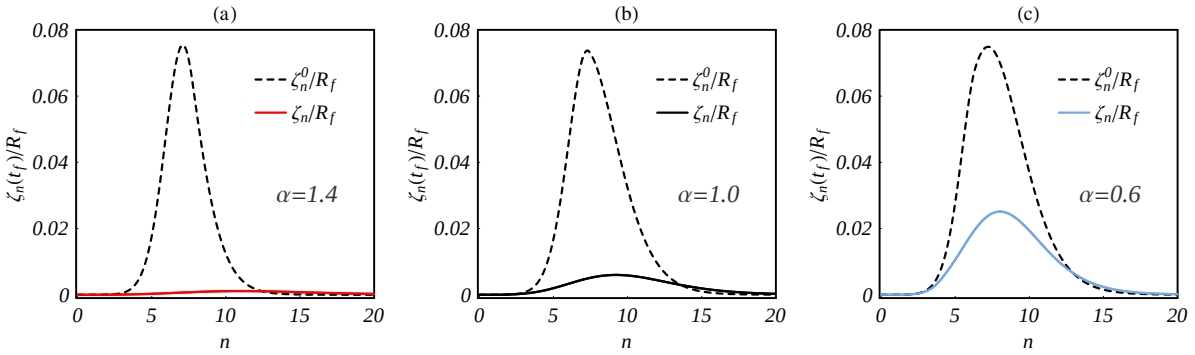

Figure 4.3 Perturbation amplitudes divided by R_f at $t = t_f$, for the optimal injection $\zeta_n(t_f)/R_f$ (solid curves) and for the equivalent constant pumping situation $\zeta_n^0(t_f)/R_f$ (dashed curves) as functions of the wave number n.

radius, the injection is no longer able to promote a considerable destabilization of the propagating front. In other words, the onset of instability is delayed, and when it eventually occurs disturbances arise with a reduced growth rate. One could say that by this reason the optimum pumping rate of the shear-thickening fluid would work in the Newtonian and shear-thinning fluids better than their own optimal pumping rates. That is not what we have observed.

The efficiency of the variational protocol can be seen even more easily in Fig. 4.4. This figure plots the interface evolution for constant injection rate (left panel), and the interface patterns for the ideal pumping situation (right panel) at $t_f = 27$ s, and equal time intervals $\Delta t = t_f/5$. Here the values considered for Q_0 and α are the same as the ones used in Fig. 4.3: [(a) and (b)] 11.1 cm^2/s and 1.4; [(c) and (d)] 2.26 cm^2/s and 1.0; and, [(e) and (f)] 1.0 cm^2/s and 0.6. The patterns in Fig. 4.4 have the same initial conditions (including the random phases attributed to each mode), and 40 modes have been considered. It is evident that finger formation is considerably inhibited on the interfaces shown on the right panel of Fig. 4.4. As we observed in Fig. 4.3, Fig. 4.4 illustrates that the minimization of the emerging fingers for shear-thickening fluids works better in comparison with the variational protocol used for shear-thinning fluids. These findings are consistent with the fact that shear-thinning (shear-thickening) has the effect of providing increasing (restraining) growth rates of fingering patterns in comparison to Newtonian fluids [41]. However, as shown in Figs. 4.4(e) and 4.4(f), our variational method is still able to considerably decrease the magnitude of interfacial disturbances, even in the shear-thinning case.

4.4 Keeping the number of fingers fixed

In this section our task is to determine what is the functional form of a time-dependent injection rate $Q(t)$ for which the number of fingers remain unchanged as time progresses. Note that in contrast to the situation examined in Sec. 4.3, here the total amount of injected fluid and the final pumping time are not fixed quantities. By using Eq. (4.13), and imposing that $n_{\max}$ is kept

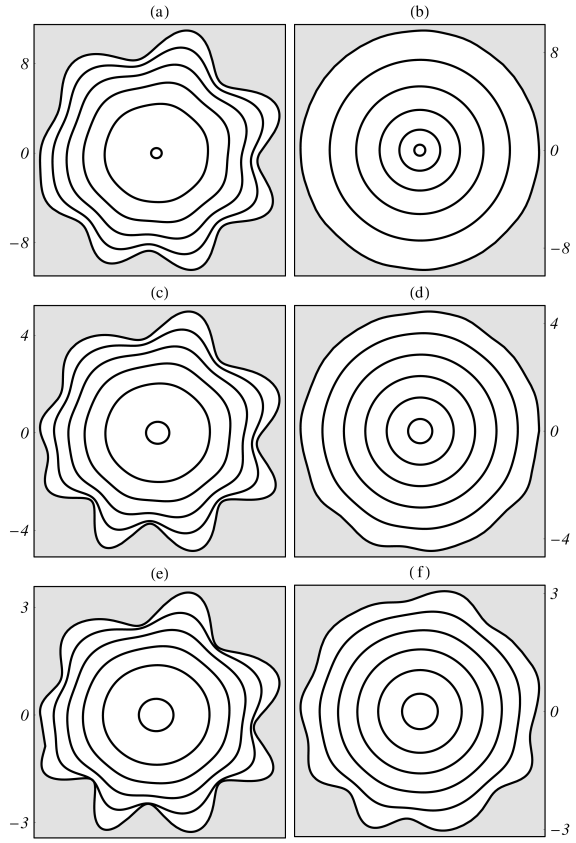

Figure 4.4 Linear time evolution of the interfacial patterns formed during constant injection rate (left column), and optimal pumping (right column) for: 11.1 cm^2/s and $\alpha = 1.4$ [(a) and (b)], 2.26 cm^2/s and $\alpha = 1.0$[(c) and (d)], and 1.0 cm^2/s and $\alpha = 0.6$ [(e) and (f)]. All computational boundaries shown are squares, and lengths are measured in units of centimeters.

unchanged yields

$$R^2\dot{R} = f(\alpha, n_{\max}), \tag{4.22}$$

where

$$f(\alpha, n_{\max}) = \left[\Gamma(\alpha)\ (3n_{\max}^2 - 1)\right]^{1/(2-\alpha)}, \tag{4.23}$$

is time-independent, and $\Gamma(\alpha)$ is given by Eq. (4.10).

Solving the differential equation (4.22) and using the fact that $Q = 2\pi R\dot{R}$ we readily obtain

$$Q(t) = 2\pi f(\alpha, n_{\max}) \left[3f(\alpha, n_{\max})t + R_0^3\right]^{-1/3}. \tag{4.24}$$

This is the adequate time-dependent injection rate needed to maintain the number of fingers fixed for viscous flow in a radial Hele-Shaw cell with a displaced power-law fluid. The corresponding Newtonian expression obtained in Refs. [26, 66–68] is recovered by setting $\alpha = 1$ in Eq. (4.24). One first noteworthy point about Eq. (4.24) is the fact that, regardless the nature of the fluid (Newtonian, shear-thinning, or shear-thickening) the proper time-dependent injection rate to control the numbers of fingers at the interface obeys the $t^{-1/3}$ dependence. All non-Newtonian effects come into play via the function $f(\alpha, n_{\max})$. This is a finding that could not

be anticipated *a priori*, since in principle a different exponent or even another functional form for $Q(t)$ could arise for the non-Newtonian situation.

Figure 4.5 illustrates how the injection rate (4.24) varies with time for three values of α and $n_{\max} = 6$. In order to control the number of emerging fingers, the shear-thickening case requires a considerably larger injection rate magnitude in comparison with the Newtonian and shear-thinning situations.

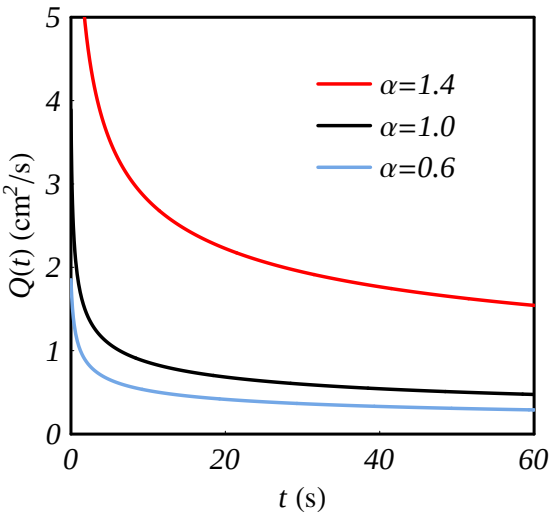

Figure 4.5 Plot of the injection rate (4.24) as a function of time, for $n_{\max} = 6$. Three values of the power-law index are considered: $\alpha = 1.4$, $\alpha = 1.0$, and $\alpha = 0.6$.

We close this section by discussing Fig. 4.6. It plots the linear evolution of the interface using the time-dependent injection rate Eq. (4.24) for α: 1.4 [Fig. 4.6(a) and Fig. 4.6(b)]; 1.0 [Fig. 4.6(c) and Fig. 4.6(d)]; and 0.6 [Fig. 4.6(e) and Fig. 4.6(f)]. All patterns have the same initial unperturbed radius R_0, and the same initial perturbation amplitude $2\times10^{-4}R_0$. These linear simulations include 40 Fourier modes, and each row [(a) and (b), (c) and (d), (e) and (f)] presents a distinct set of random phases. The column on the left (right) considers that $n_{\max} = 6$ ($n_{\max} = 8$). First, we can verify that for a fixed initial condition we can choose the number of emerging fingers at the interface just by manipulating the injection rate provided by Eq. (4.24). Furthermore, it is apparent that the control of the number of fingers is eventually achieved regardless the value of the power law index α.

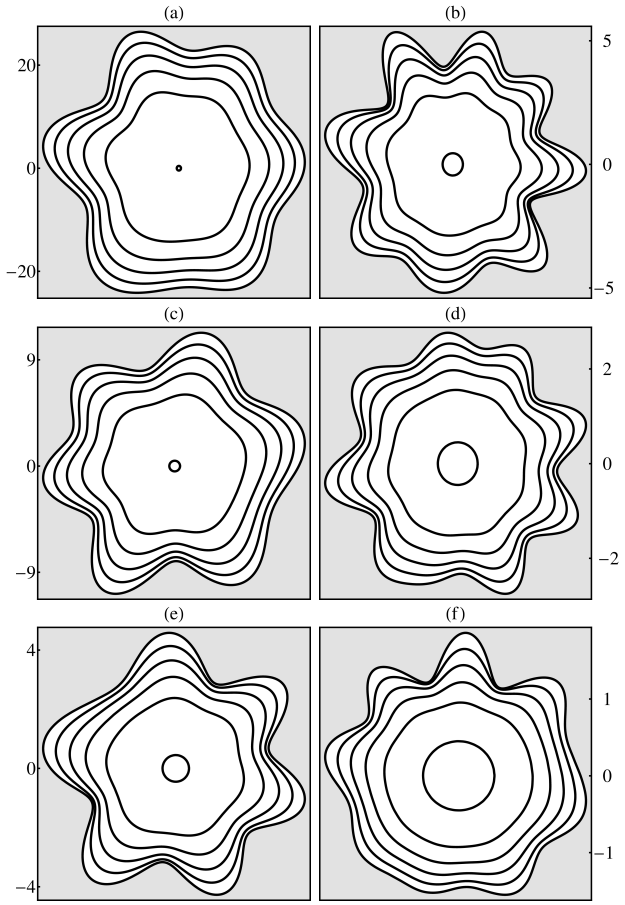

Figure 4.6 Linear time evolution of the interfacial patterns formed during the time-dependent injection rate (4.24), for $n_{\max} = 6$ (left column) and $n_{\max} = 8$ (right column). Here we set $\alpha = 1.4$ [(a) and (b)], $\alpha = 1.0$ [(c) and (d)], and $\alpha = 0.6$ [(e) and (f)]. The final times used are: (a) 3.2×10^3 s, (b) 9 s, (c) 1.2×10^3 s, (d) 12 s, (e) 1.5×10^2 s, and (f) 6 s. All computational boundaries shown are squares, and lengths are measured in units of centimeters.

CHAPTER 5

Conclusion

Since only a relatively smaller part of the fluids of academic and technological interest are Newtonian it is natural to make an effort to understand how the well known HSC problem behaves when a non-Newtonian behavior comes into play. There are several theoretical and experimental evidences that the rheology of the fluids have a deep influence on the stability and morphology of the emerging patterns. In this work we have performed a theoretical study to gain analytical insight into this influence.

In chapter 2 we have considered a modified version of the Saffman-Taylor viscous fingering problem in radial Hele-Shaw geometry. In contrast to the conventional purely Newtonian situation, we have examined the case in which a fluid of negligible viscosity displaces a viscous yield stress fluid. Motivated by existing experiments [47, 48] we have focused on the regime in which viscous effects prevail over yield stress. These experiments revealed the rising of ramified structures, presenting some tip-splitting events, but the predominance of side branching phenomena.

In order to get some analytical insight into the onset of pattern formation we have derived two main theoretical results: first, using the lubrication approximation we deduced a Darcy-like law for the gap-averaged problem. Then, by employing a perturbative weakly nonlinear approach we have found the mode-coupling differential equation which governs the time evolution of the interface at lowest nonlinear order. In this framework, we have shown that consideration of the coupling between a small number of modes allows one to predict and detect the occurrence of both tip-splitting and side branching.

Finger widening and splitting occur through the favored growth of the harmonic mode $2n$, while side branching develops through the enhanced growth of mode $3n$. Nonlinear mode-coupling enhances the growth of these specific perturbations with appropriate relative phases. Lastly, we provided a morphological phase diagram that shows the flow and fluid parameters required to develop either tip-splitting or side branching. In conclusion, in chapter 2 we have developed a relatively simple analytical model which is able to capture the most salient features of this interesting and complex pattern formation problem.

In addition to injection-driven flows in constant-gap HSC, there are several experimental and theoretical studies on the lifting flow problem in the confined geometry of a variable-gap HSC. Most of these investigations focus on understanding purely linear, early time dynamic stages of the problem, or its advanced time, fully nonlinear dynamics. Researchers consider that an inner fluid (which can be Newtonian or non-Newtonian) is surrounded by another fluid of much smaller viscosity. Under lifting flow circumstances, the fluid-fluid interface deforms, producing a variety of complex interfacial patterns. On the theoretical side, the study of such complicated patterns is usually performed by analytical linear stability analyses, or by sophis-

ticated numerical simulations.

In chapter 3 we studied the linear and nonlinear dynamics of a yield stress fluid located in a lifting HSC, focusing in the regime of viscous effects prevailing over yield stress. We used the same Darcy-like law and perturbative weakly nonlinear approach used in chapter 2 that allows analytic access not only to linear stability issues, but also to key nonlinear aspects of the interface morphology. We derived a nonlinear differential equation describing the time evolution of the perturbation amplitudes. This equation has been utilized to describe finger competition phenomena in lifting HSC in terms of two dimensionless controlling parameters: the geometric aspect ratio q (a measure of the HSC confinement), and the yield stress parameter δ (relative measure of yield stress to viscous forces). Our results indicate that while $\delta > 0$ tends to restrain finger competition of inward moving fingers of the penetrating outer fluid, larger values of q (great confinement) enhance competition among these fingering structures. These conclusions are in general agreement with existing experimental studies [52, 53, 55].

Then we turned our attention to control process in HSC with non-Newtonian fluids.It is known that the displacement of liquids from confined geometries by using a gas phase is an important problem to many technologies. In this context, hydrodynamic instabilities can turn the process inefficient and uneconomical. Therefore, it is necessary to develop ways of reducing or eliminating the detrimental effects of viscous instabilities to make this type of processes economically viable even under adverse conditions. The academic counterpart of this practical situation involves the displacement of a viscous fluid by a less viscous one in the spatially constrained geometry of a HSC. Efficient removal of the more viscous phase is achieved when the development of such instabilities is inhibited. Most existing studies that somehow try to control the emergence of these interfacial disturbances consider that the displaced fluid is Newtonian. An improved understanding of the link between non-Newtonian flow properties and interfacial instability will certainly improve the selection guidelines for controlling protocols on the scientific level, and hopefully provide a basis for future technological applications.

Motivated by these facts, in chapter 4 we considered the displacement of a viscous non-Newtonian (power-law) fluid by an inviscid fluid in a radial Hele-Shaw cell. First, for the case in which the total amount of injected fluid is fixed, we employed a variational approach for obtaining the optimal injection process, i.e., the policy which minimizes the growth of the viscous fingering instability. In this case, we have found that the optimization process is substantially dependent on the power law index. Then, considering that the total amount of injected fluid is not fixed, we focused on searching for a time-dependent injection process that intended to control the total number of resulting fingers arising at the interface. We have found that regardless the nature of the displaced fluid (Newtonian, shear-thinning, or shear-thickening) the desired injection rate scales as $Q(t) \sim t^{-1/3}$, but with a proportionality constant that depends on the power law index α. The efficiency of these two different controlling strategies has been verified through linear simulations of the early time stages of the interface dynamics.

The theoretical work presented in chapter 4 makes specific predictions that have not yet been subjected to experimental or fully nonlinear numerical check. In the case of earlier controlling studies involving a Newtonian displaced fluid [26, 66, 67, 71], linear predictions have indeed been supported by long-time laboratory experiments and fully nonlinear numerical simulations. For instance, the time-dependent injection rate $Q(t) \sim t^{-1/3}$ predicted in

Refs. [26, 66] by a simple linear stability analysis, ended up suppressing key nonlinear effects (i.e., finger tip-splitting and finger competition), revealing self-similar structures in Newtonian fluids at advance time regime [26, 67]. The same was also true for the linear stability based variational protocol proposed in Ref. [71], where the predicted strong stabilization of the interfacial amplitudes has been substantiated by experiments and intensive nonlinear simulations. Therefore, it would be of interest to examine the robustness and validity of the proposed non-Newtonian controlling and minimizing protocols presented here for advanced times. A possible extension of the work presented in chapter 4 would be the investigation of similar controlling and minimizing techniques for other complex fluids, such as viscoelastic and yield-stress fluids [42, 43, 46–48, 78], in which important effects like elasticity and plasticity must be taken into account.

We hope the work carried out in this dissertation will instigate further theoretical and experimental studies on the challenging but rich research topic of HSC flow with non-Newtonian fluids.

Bibliography

[1] L. A. Segel, Mathematical Models of Molecular and Cellular Biology (CambridgeUniversity Press, 1980).

[2] P. G. Saffman and G. I. Taylor, Proc. R. Soc. London Ser. A **245**, 312 (1958).

[3] H. Meinhardt, Models of Biological Patterns Formation (Academic Press, New York, 1982).

[4] A. C. Callan-Jones, J.-F. Joanny e J. Prost, Phys. Rev. Lett. **100**, 258106 (2008).

[5] B. Chalmers, Principles of solidification (Wiley, New York, 1964).

[6] J. V. Maher, Phys. Rev. Lett. **54**, 1498 (1985).

[7] G. Tryggvason and H. Aref, J. Fluid Mech. **136**, 1 (1983).

[8] A. J. DeGregoria and L. W. Schwartz, J. Fluid Mech. **164**, 383 (1986).

[9] E. Meiburg and G. M. Homsy, Fluids **31**, 429 (1988).

[10] C. -W. Park and G. M. Homsy, Phys. Fluid **28**, 1583 (1985).

[11] P. Tabeling, G. Zocchi and A. Libchaber, J. Fluid Mech. **177**, 67 (1987).

[12] T. Maxworthy, J. Fluid Mech. **177**, 207 (1987).

[13] A. Arnéodo, Y. Couder, G. Grasseau, V. Hakim and M. Rabaud, Phys. Rev. Lett. **63**, 984 (1989).

[14] J. A. Miranda and M. Widom, Int. J. Mod. Phys. B **12**, 931 (1998).

[15] J. Bataille, Rev. Inst. Fr. Pet. Ann. Combust. Liq. **23**, 1349 (1968).

[16] S. D. R. Wilson, J. Colloid Interface Sci. **51**, 532 (1975).

[17] O. Praud and H. L. Swinney, Phys. Rev. E **72**, 011406 (2005).

[18] P. Fast and M. J. Shelley, J. Comput. Phys. **212**, 1 (2006).

[19] J. Mathiesen, I. Procaccia, H. L. Swinney, and M. Thrasher, Eur. Phys. Lett. **76**, 257 (2006).

[20] S. W. Li, J. S. Lowengrub, and P. H. Leo, J. Comput. Phys. **225**, 554 (2007).

[21] C.-Y. Chen, C.-W. Huang, H. Gadêlha, and J. A. Miranda, Phys. Rev. E **78**, 016306 (2008).

[22] L. Paterson, J. Fluid Mech. **113**, 513 (1981).

[23] J.-D. Chen, J. Fluid Mech. **201**, 223 (1989); J. -D. Chen, Exp. Fluids **5**, 363 (1987).

[24] H. Thomé, M. Rabaud, V. Hakim, and Y. Couder, Phys. Fluids **A1**, 224 (1989).

[25] J. A. Miranda and M. Widom, Physica D **120**, 315 (1998).

[26] S. W. Li, J. S. Lowengrub, J. Fontana, and P. Palffy-Muhoray, Phys. Rev. Lett. **102**, 174501 (2009).

[27] R. B. Bird, R. Armstrong, and O. Hassager *Dynamics of Polymeric Liquids* (Wiley, New York, 1977).

[28] A. Buka, P. Palffy-Muhoray, and Z. Racz, Phys. Rev. A **36**, 3984 (1987).

[29] H. Zhao and J. V. Maher, Phys. Rev. E **47**, 4278 (1993).

[30] J. Ignés-Mullol, H. Zhao and J. V. Maher, Phys. Rev. E **51**, 1338 (1995).

[31] N. Kagei, D. Kanie, and M. Kawaguchi, Phys. Fluids **17**, 054103 (2005).

[32] D. Bonn, H. Kellay, M. Ben Amar and J. Meunier, Phys. Rev. Lett. **75**, 2132 (1995); D. Bonn, H. Kellay, M. Braunlich, M. Ben Amar, and J. Meunier, Physica A **220**, 60 (1995).

[33] L. Kondic, P. Palffy-Muhoray, and M. J. Shelley, Phys. Rev. E **54**, R4536 (1996).

[34] L. Kondic, M. J. Shelley, and P. Palffy-Muhoray, Phys. Rev. Lett. **80**, 1433 (1998).

[35] E. Corvera Poiré and M. Ben Amar, Phys. Rev. Lett. **81**, 2048 (1998).

[36] M. Ben Amar and E. Corvera Poiré, Phys. Fluids **11**, 1757 (1999).

[37] P. Fast and M. J. Shelley, J. Comput. Phys. **195**, 117 (2004).

[38] S. Nguyen, R. Folch, V. K. Verma, H. Henry, and M. Plapp, Phys. Fluids **22**, 103101 (2010).

[39] M. Constantin, M. Widom, and J. A. Miranda, Phys. Rev. E **67**, 026313 (2003).

[40] P. Fast, L. Kondic, M. J. Shelley, and P. Palffy-Muhoray, Phys. Fluids **13**, 1191 (2001).

[41] J. E. Sader, D. Y. C. Chan, and B. D. Hughes, Phys. Rev. E **49**, 420 (1994).

[42] H. A. Barnes, J. Non-Newtonian Fluid Mech. **81**, 133 (1999).

[43] P. Moller, A. Fall, V. Chikkadi, D. Derks, and D. Bonn, Phil. Trans. R. Soc. A **367**, 5139 (2009).

[44] Q. Barral, G. Ovarlez, X. Chateau, J. Boujlel, B. Rabideau, and P. Coussot, Soft Matter **6**, 1343 (2010).

[45] P. Coussot, J. Fluid Mech. **380**, 363 (1999).

[46] E Lemaire, P. Levitz, G. Daccord, and H. Van Damme, Phys. Rev. Lett. **67**, 2009 (1991).

[47] A. Lindner, P. Coussot, and D. Bonn, Phys. Rev. Lett. **85**, 314 (2000).

[48] N. Maleki-Jirsaraei, A. Lindner, S. Rouhani, and D. Bonn, J. Phys.: Condens. Matter **17**, S1219 (2005).

[49] G. M. Homsy, Annu. Rev. Fluid Mech. **19**, 271 (1987); K. V. McCloud and J. V. Maher, Phys. Rep. **260**, 139 (1995); J. Casademunt, Chaos **14**, 809 (2004).

[50] M. J. Shelley, F-R. Tian, and K. Wlodarski, Nonlinearity **10**, 1471 (1997).

[51] M. Ben Amar and D. Bonn, Physica D **209**, 1 (2005).

[52] D. Derks, A. Lindner, C. Creton, and D. Bonn, J. Appl. Phys. **93**, 1557 (2003).

[53] A. Lindner, D. Derks, and M. J. Shelley, Phys. Fluids **17**, 072107 (2005).

[54] J. Nase, A. Lindner, and C. Creton, Phys. Rev. Lett. **101**, 074503 (2008).

[55] J. Nase, D. Derks, and A. Lindner, Phys. Fluids **23**, 123101 (2011).

[56] S. Poivet, F. Nallet, C. Gay, J. Teisseire, and P. Fabre, Eur. Phys. J. E **15**, 97 (2004).

[57] Y.O.M. Abdelhaye, M. Chaouche, and H. Van Damme, Appl. Clay Sci. **42**, 163 (2008).

[58] S. Sinha, T. Dutta, and S. Tarafdar, Eur. Phys. J. E **25**, 267 (2008).

[59] C.-Y. Chen, C.-H. Chen, and J. A. Miranda, Phys. Rev. E **71**, 056304 (2005).

[60] R. M. Oliveira and J. A. Miranda, Phys. Rev. E **73**, 036309 (2006).

[61] S. B. Gorell and G. M. Homsy, SIAM J. Appl. Math. **43**, 79 (1983); J. P. Stokes, D. A. Weitz, J. P. Gollub, A. Dougherty, M. O. Robbins, P. M. Chaikin, and H. M. Lindsay, Phys. Rev. Lett. **57**, 1718 (1986).

[62] D. Cherrak, E. Guernet, P. Cardot, C. Herrenknecht, and M. Czok, Chromatographia **46**(1), 647 (1997).

[63] G. Rousseaux, A. De Wit, and M. Martin, J. Chromatogr. A **1149**(2), 254 (2007).

[64] L. W. Schwartz and R. V. Roy, Phys. Fluids **16**, 569 (2004).

[65] K. E. Holloway, P. Habdas, N. Semsarillar, K. Burfitt, and J. R. de Bruyn, Phys. Rev. E **75**, 046308 (2007).

[66] S. S. S. Cardoso and A. W. Woods, J. Fluid Mech. **289**, 351 (1995).

[67] A. Leshchiner, M. Thrasher, M. B. Mineev-Weinstein, and H. L. Swinney, Phys. Rev. E **81**, 016206 (2010).

[68] C.-Y. Chen, C.-W. Huang, L.-C. Wang, and J. A. Miranda, Phys. Rev. E **82**, 056308 (2010).

[69] E. O. Dias and J. A. Miranda, Phys. Rev. E **81**, 016312 (2010).

[70] E. O. Dias, F. Parisio, and J. A. Miranda, Phys. Rev. E **82**, 067301 (2010).

[71] E. O. Dias, E. Alvarez-Lacalle, M. S. Carvalho, and J. A. Miranda, Phys. Rev. Lett. **109**, 144502 (2012).

[72] D. Pihler-Puzović, P. Illien, M. Heil, and A. Juel, Phys. Rev. Lett. **108**, 074502 (2012).

[73] D. Pihler-Puzović, R. Périllat, M. Russell, A. Juel, and M. Heil, J. Fluid Mech. **731**, 162 (2013).

[74] T. T. Al-Housseiny, I. C. Christov, and H. A. Stone, Phys. Rev. Lett. **111**, 034502 (2013).

[75] T. T. Al-Housseiny, P. A. Tsai, and H. A. Stone, Nature Phys. **8**, 747 (2012).

[76] R. M. Wilson, Phys. Today **65**(10), 15 (2012).

[77] T. T. Al-Housseiny and H. A. Stone, Phys. Fluids **25**, 092102 (2013).

[78] J. V. Fontana, S. A. Lira, and J. A. Miranda, Phys. Rev. E **87**, 013016 (2013).

[79] S. D. R. Wilson, J. Fluid Mech. **220**, 413 (1990).

[80] V. A. Gorodtsov and V. M. Yentov, J. Appl. Math. Mech. **61**, 111 (1997).

[81] S. Mora and M. Manna, Phys. Rev. E **80**, 016308 (2009).

[82] S. W. McCue and J. R. King, Nonlinearity **24**, 613 (2013).

[83] J. V. Fontana and J. A. Miranda, Phys. Rev. E **88**, 023001 (2013).

[84] J. V. Fontana, E. O. Dias, and J. A. Miranda, Phys. Rev. E (accepted 2013).

[85] J. V. Fontana and J. A. Miranda, Phys. Rev. E **88**, 063003 (2013).

[86] G. K. Batchelor, *An Introduction to Fluid Dynamics* (Cambridge University Press, Cambridge, 1967).

[87] G. Dai and R. B. Bird, J. Non-Newtonian Fluid Mech. **8**, 349 (1981).

[88] M. J. P. Gingras and Z. Rácz, Phys. Rev. A **40**, 5960 (1989).

[89] O. Perron, Math. Z. **32**, 703 (1930).

[90] M. C. Dallaston and S. W. McCue, Nonlinearity **26**, 1639 (2013).

[91] R. B. Bird, R. Armstrong, and O. Hassager *Dynamics of Polymeric Liquids* (Wiley, New York, 1977).

[92] M. Abramowitz and I. A. Stegun, *Handbook of Mathematical Functions with Formulas, Graphs, and Mathematical Tables* (Dover, New York, 1972).

APPENDIX A

Derivation of n_{max} for the yield stress fluid in a injection-driven HSC, equation (2.46)

This appendix describes the main steps of the derivation of Eq. (2.46). By using Eq. (2.35) and setting $[d\lambda(n)/dn]_{n=n_{max}} = 0$ for the situation in which $\delta \neq 0$, we obtain a complicated equation for n_{max}

$$\frac{1}{R^2} - \frac{\Gamma}{R^3}(3n_{max}^2 - 1) + \delta\left\{\frac{(2n_{max}^2 - 2n_{max} + 1)}{(2n_{max} - 1)^2}\left(\frac{1}{R}\right)\right.$$
$$\left. + \left(\frac{\Gamma}{R^2}\right)\frac{2n_{max}(3n_{max}^3 - 2n_{max}^2 - n_{max} + 1)}{(2n_{max} - 1)^2}\right\} = 0. \tag{A.1}$$

By considering the limit $\Gamma \ll 1$, so that the product $\delta\Gamma$ is negligibly small, Eq. (A.1) can be rewritten in a much simpler form

$$\frac{\Gamma}{R}(3n_{max}^2 - 1) = 1 + \delta R\left\{\frac{2n_{max}^2 - 2n_{max} + 1}{(2n_{max} - 1)^2}\right\}. \tag{A.2}$$

Recalling that we only consider contributions up to first order in δ, notice that on the right hand side of Eq. (A.2) we can replace n_{max} by n_{max}^N [Eq. (2.45)] without loss of generality. In this context, and assuming that $(n_{max}^N)^2 \gg n_{max}^N \gg 1$, we may approximate $(2n_{max}^2 - 2n_{max} + 1)/(2n_{max} - 1)^2 \approx 1/2$. Thus, Eq. (A.2) is simplified further, leading to

$$n_{max} = \sqrt{\frac{R}{3\Gamma}}\left(1 + \frac{\Gamma}{R} + \frac{\delta R}{2}\right)^{1/2}. \tag{A.3}$$

By utilizing this equation plus Newton's generalized binomial theorem [92]

$$(x+y)^r = x^r + rx^{r-1}y + \ldots \tag{A.4}$$

where $x = 1 + \Gamma/R$, $y = \delta R/2$, and $r = 1/2$ we get

$$\begin{aligned} n_{max} &= \sqrt{\frac{R}{3\Gamma}}\left[\sqrt{1 + \frac{\Gamma}{R}} + \frac{\delta R}{4}\frac{1}{\sqrt{1 + \frac{\Gamma}{R}}} + \mathscr{O}(\delta^2)\right] \\ &= \sqrt{\frac{1}{3}\left(1 + \frac{R}{\Gamma}\right)} + \frac{\delta R}{4}\frac{\sqrt{\frac{R}{3\Gamma}}}{\sqrt{1 + \frac{\Gamma}{R}}}. \end{aligned} \tag{A.5}$$

By considering the situation $\Gamma \ll 1$, we may write $(1+R/\Gamma) \approx R/\Gamma$ and $(1+\Gamma/R) \approx 1$. Then, Eq. (A.5) leads to

$$n_{max} \approx \sqrt{\frac{1}{3}\left(1+\frac{R}{\Gamma}\right)}\left(1+\frac{\delta R}{4}\right). \tag{A.6}$$

With the help of Eq. (2.45), this last expression readily leads to Eq. (2.46).